Wave Optics Simulation of Subwavelength Structures within Solar Cells

Integration of RCWA with GenPro4

Ivo Smink

Technische Universiteit Delft

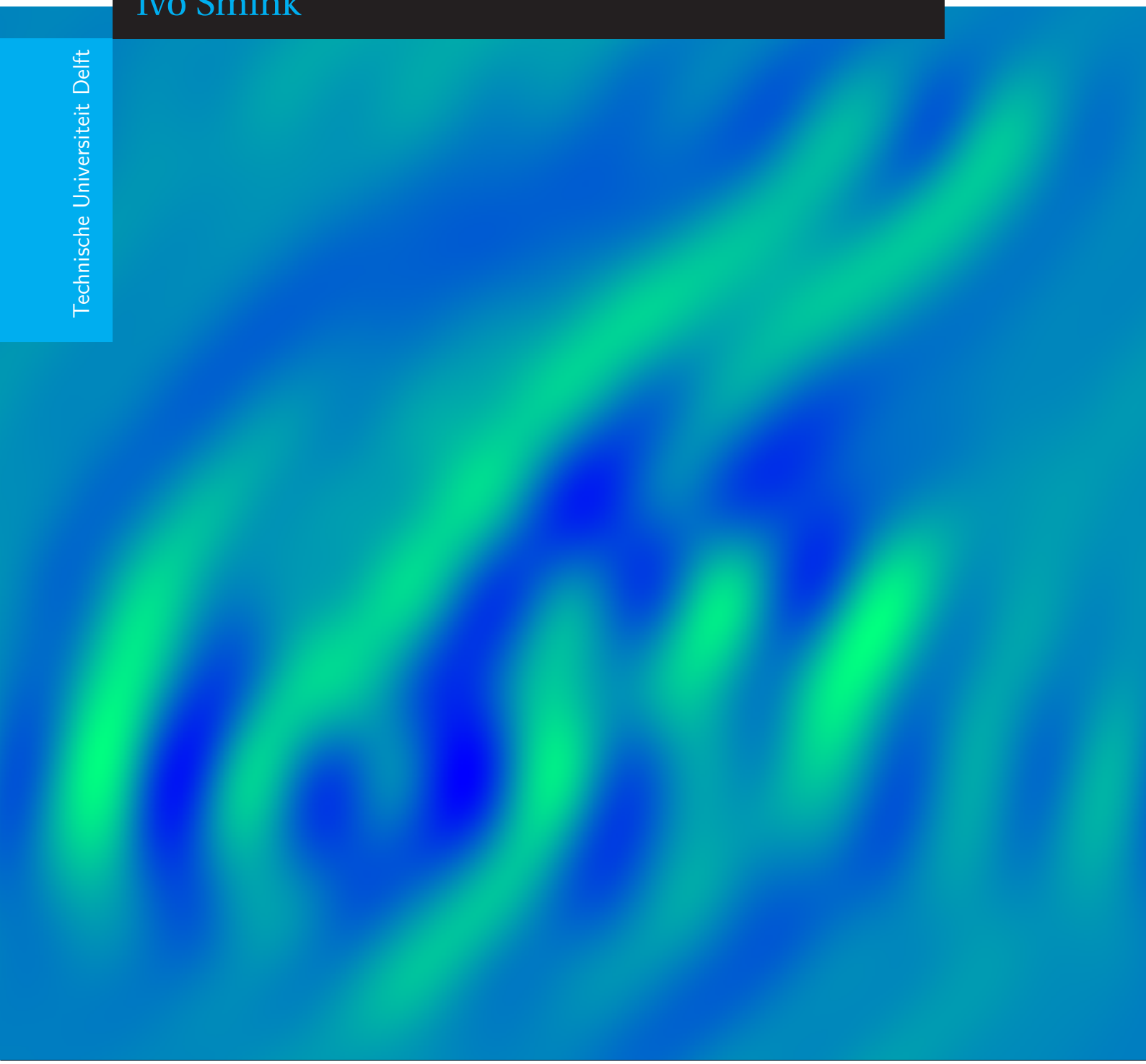

TU Delft Delft University of Technology

Challenge the future

Wave Optics Simulation of Subwavelength Structures within Solar Cells

Integration of RCWA with GenPro4

by

Ivo Smink

to obtain the degree of Master of Science

at the Delft University of Technology,

to be defended publicly on Wednesday October 25, 2021 at 2:00 PM.

Student number:	4352327	
Project duration:	February 8, 2021 – October 25, 2021	
Thesis committee:	Dr. R. Santbergen,	TU Delft, supervisor
	Dr. R.A.C.M.M. Swaaij,	TU Delft
	Dr. N. Bhattacharya,	TU Delft

An electronic version of this thesis is available at http://repository.tudelft.nl/.

TU Delft

Abstract

To further improve the light management and optical performance of solar cells, research into nano-textured interfaces has led to a need for a fast and accurate wave optics model. Currently, within the PVMD group at the TU Delft a optical solar cell simulation tool, GenPro4, is being developed to allow for the quick optimization and analysis of solar cell designs. However, the implemented wave optics model has limited accuracy and thus an alternative model is sought.

In this thesis, we researched several rigorous wave optics simulation methods such as: finite element method, finite difference time domain, transfer matrix method, and rigorous coupled wave analysis. Based on three decision criteria (speed, accuracy, and compatibility) the choice of implementing rigorous coupled wave analysis (RCWA) was made. Besides the standard RCWA formulations a few improvements were made. S-matrices were used to increase speed and memory efficiency of the program. Furthermore, calculation of the local E-field allowed for the determination of absorption per material in our cell. Lastly, an angular intensity distribution, known as scatter matrix, was produced as output to allow for the full integration with GenPro4.

We validated our new model by comparing results of a nano-textured GICS solar cell with previously conducted finite element method (FEM) simulations. Over a large wavelength range our model showed good agreement with the FEM data. However, slight inaccuracies were observed at longer wavelengths (>1000 nm) as simulation of the metal back reflector became infeasible. Highly absorbing materials, such as metals, potentially required several hundred Fourier modes to be modeled accurately. However, simulations with such a high number of Fourier modes is not feasible as the computer resources (RAM) and computational time needed grow exponentially. Furthermore, for very small textures, RCWA converges with the GenPro4 flat model as is expected for sufficiently small textures.

Nevertheless, integration of RCWA with GenPro4 was achieved. To demonstrate the ability to quickly and easily simulate real work cell designs, a case study of a perovskite/silicon tandem cell was conducted. In the case study a combination of 16 interface mythologies was simulated and compared. With the optimal combination showing a potential improvement of 2% over the reference cell.

Preface

This thesis has been written as the final part of my master degree in Sustainable Energy Technology at the Delft University of Technology. For about eight months I have put my heart and soul into this project. Even through these trying times, during the lockdown, I have greatly enjoyed the opportunity I have been given to be part of the PVMD group. It has been very interesting to see how much research is being done in, what I believe to be, the future energy source that is solar. I have never been more confident in our ability to transition to a carbon neutral future than today.

There are a few people I would like to thank for their support during this thesis project. First, Rudi Santbergen for all positive and critical feedback on my work. Nasim Rezaei for the FEM data need for my validation. Additionally, Merel for the much needed emotional support and discussions, even if I did have the tendency to ramble on a bit. And, of course, Zenna for all the long walks that helped me stay grounded, even if you didn't.

Lastly, there are people that have done more than just supported me during this time, and I would like to thank them as well for helping me become the person I am today. Mom, Dad, Teddie, Sasha, Jeffrey, Lisanne, Hans, Wiep, David, Oscar, Max K., Anne, Caroline, Toni, Laura, and all of Wave H1: from the bottom of my heart, thank you!

Ivo Smink
Delft, October 2021

Contents

Nomenclature

Acronyms

V	Eigenvector matrix of magnetic field
W	Eigenvector matrix of electric field
ϵ_o	Permittivity free space
ϵ_r	Relative Permittivity
μ_r	Relative Permeability
$\vec{E}$	Electric Field
$\vec{H}$	Magnetic Field
C_b	Backwards propagating mode coefficients
C_f	Forwards propagating mode coefficients
$e_{x,y,z}$	Electric field amplitudes of the spacial harmonics in Fourier space
$h_{x,y,z}$	Magnetic field amplitudes of the spacial harmonics in Fourier space
k_0	Free space wave number
S^i	S-matrix of layer i
S^{global}	Global S-matrix of entire device
λ	wavelength
AID	Angular Intensity Distribution
ARC	Anti-Reflective Coating
FDTD	Finite Difference Time Domain
FEM	Finite Element Method
FFT	Fast Fourier Transform
$K_{x,y}$	x,y directional wave number
$P_{x,y}$	Period along x,y direction
RCWA	Rigorous Coupled Wave Analysis
S-matrix	Scatter matrix used in the coupling input modes to output modes
SSM	Scalar scattering model
SWS	Sub-Wavelength Structures

TMM	Transfer Matrix Method
Z_0	Impedance Free Space

1

Introduction

Solar cell technology has made incredible advancements in the last decades. Due to constant improvements, researchers have been able to produce a single junction c-Si solar cell with a record efficiency of 26.7% [1]. We are now several percentage points from the theoretical limit set by William Shockley and Hans Queisser back in 1961 of 33% [2]. This is, in part, thanks to the improved light trapping and management techniques current solar cell manufacturers use.

Solar cells are dependant on the absorption of photons to generate energy. When light falls incident on a medium with a different index of refraction it is split into a reflected and transmitted beam, as was first described by Augustin Jean Fresnel in 1821 [3]. Ideally, for a solar cell, all light would be transmitted and none would be reflected thus allowing all photons to be absorbed and generate electricity. However, this is not physically possible. Two methods are often used to limit the reflective losses: anti-reflective coatings (ARC) and surface texturing. To develop the best solar cell design, understanding of how light interacts with these ARCs and textures is crucial. Often times, computer models are used to optimize the thickness of coating and dimensions of textures as this eliminates the need for expnsive and time consuming experimental measurements.

1.1. Solar Cell Optical Modeling

A solar cell needs to perform under a range of wavelengths and incident angles. Computer modeling has been used to determine how a solar cell design performs under all these circumstances. Within the Photovoltaic Materials and Devices (PVMD) group of the TU Delft an optical model for solar cell is being developed, known as GenPro4 [4]. This model is aimed at providing a quick and accurate way of modeling optical effects in solar cells. Large micro-textures are modeled using ray optics, where light is represented as a infinitely thin ray. These large, with respect to the wavelength of light, structures are modeled using the ray tracer fully integrated in GenPro4.

Recently, improvements in solar cell manufacturing have allowed for the manufacturing of so called sub-wavelength structures (SWS). As the name suggests, the dimensions of these surface textures are at or below the wavelength of the incident light. This has the benefit of limiting reflections and diffracting light into large angles to increase the absorption in the layers below [5]. However, unlike the larger macro-statures, these much smaller nano-structures can

not be modeled using the same ray optics. Due to the size in relation to the wavelength of light incident, wave optics need to be used to simulate this interaction accurately. This is done by modeling the electromagnetic waves-material interaction through the solving of Maxwell's equations.

Integrated in GenPro4 is a wave optics model known as the scalar scattering model developed by Jäger [6]. Although this model can quickly generate a solution for the wave interaction with SWS, it lacks accuracy in a variety of situations as it does not directly solve Maxwell's equations [4], as will be further explained in chapter 2. Therefore, a more rigorous model is desired to overcome these limitations and provide a robust model for all SWS within a solar cell.

In the last decades, computer processing power has increased significantly. Complex simulations such as optical modeling for solar cells, as introduced above, have now become possible. This has led to numerous methods, previously not computationally stable or feasible with historic computer resources, now gaining popularity [7, 8].

1.2. Research Goal and Thesis Outline

To further optimize solar cell performance, optical modeling is used to gain insight in the effect of cell structures on performance. GenPro4 aims to quickly and accurately model any solar cell design with either ray or wave optics. However, currently, the wave optics model is limited in accuracy and an alternative is desired. This leads to the research goal of this master thesis:

Research and implement an improved wave optics model into GenPro4.

To achieve this the following questions will be addressed:

- Which alternative wave optics model is best suited for integration with GenPro4?
- Can any speed or accuracy improvements be made?
- What computational or accuracy limits, if any, does the new model face?

In chapter 2, an overview of GenPro4, the current wave model, and alternative wave models is given. Followed by chapter 3, where the chosen wave model is further explained and then validated in chapter 4. Additionally, a case study of the fully integrated new wave model will be given in chapter 5. Lastly, concluding remarks and recommendations will be given in chapter 6.

2

Optical Models

In this chapter we will first discuss the different methods used to manage light within a solar cell. Next, a review of the optical solar cell software GenPro4 as well as the current wave optics model (Scalar scatter model, 2.2.1) will be given. This is followed by a brief overview of alternative wave models. Lastly, an alternative model will be chosen based on a few criteria, namely: speed, accuracy, and compatibility.

2.1. Light Management in Solar Cells

The understanding of how light interacts with solar cells is crucial to develop an optimal cell structure. Throughout the last few decades, researchers have gained great insight into different methods of managing the light to allow for limited reflections and better absorption in specific layers. Ideally, for a solar cell, all light would be transmitted and none would be reflected thus allowing all photons to be absorbed and generate electricity. However, this is not physically possible. Two methods are often used to limit the reflective losses: anti-reflective coatings (ARC) and surface texturing. Both techniques will be discussed and compared in the following subsections.

2.1.1. Anti-reflective coatings

The Fresnel equation for reflection at normal incidence ($\theta = 0$) is given by equations 2.1 below [9].

$$R = \left| \frac{n_1 - n_2}{n_1 + n_2} \right|^2 \tag{2.1}$$

Reflectively is dependent on the relative difference in the index of refraction between the first medium n_1 and the second medium n_2. ARCs can help minimize reflections by acting as an intermediate layer between two layers with different index of refraction. A material with an index of refraction equal to the geometric mean of the two adjacent materials is ideal. Equation 2.2 shows this relation, with n being the index of refraction of the new intermediate ARC layer.

$$n = \sqrt{n_1 * n_2} \tag{2.2}$$

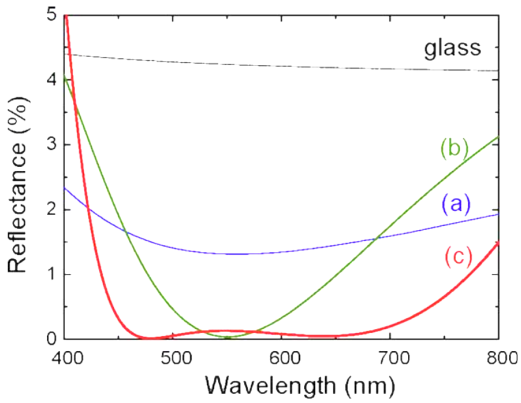

Figure 2.1: Reflection values for glass, single layer ARC (a), double layer ARC (b), triple layer ARC (c) [9]

Additionally, interference properties of light can be used to further minimize the reflectance at the front surface of this intermediate layer. When two perfectly out of phase light waves interact, they cancel each other out; this is known as destructive interference. This occurs at an ARC optical thickness of a quarter wavelength ($\frac{\lambda}{4}$), and therefore is known as the quarter wavelength rule [10].

Unfortunately, this only eliminates the reflections for one wavelength of light. Therefore, ARC are often chosen to have thickness of 125 nm to target the peak of the AM1.5 solar spectrum of 500 nm [10]. Multiple coatings can also be applied to the front surface of the solar cell to further improve the optical performance. This does come at an increased cost and still produces high reflection values for a few wavelengths as can be seen in figure 2.1. ARCs can also lead to parasitic absorption which, just like reflection, lowers the performance of the solar cell.

2.1.2. Texturing

Surface texturing is often used to limit reflections as well as increase the light trapping properties of solar cells. By etching away portions of the surface, a non-flat interface can be created. When light falls onto a non-flat surface it's reflectance, and thus also it's transmittance, becomes a function of the angle of incidence, as can be seen in equation 2.3.

$$R = \left| \frac{n_1 * cos(\theta_i) - n_2 * cos(\theta_t)}{n_1 * cos(\theta_i) + n_2 * cos(\theta_t)} \right|^2 \tag{2.3}$$

This equation is similar to equation 2.1, but now we also introduce an incident and transmission angle, θ_i and θ_t respectively. The transmittance angle can be calculated by using Snell's law for every incident angle:

$$n_1 sin(\theta_i) = n_2 sin(\theta_t) \tag{2.4}$$

This angle dependence of reflection allows for the manufacturing of specific front surface textures that allows for the reflection of light into adjacent surfaces and then back into the absorbent layer, as can be seen in figure 2.2. Light trapping can also take place when the incident angle is above a critical value, this is known as total internal reflection, and is seen as secondary benefit of surface texturing. Pyramid micro structures, such as the ones visible in figure 2.2, in combination with ARCs have proven to be able to reduce reflection to below 2% [11]. These

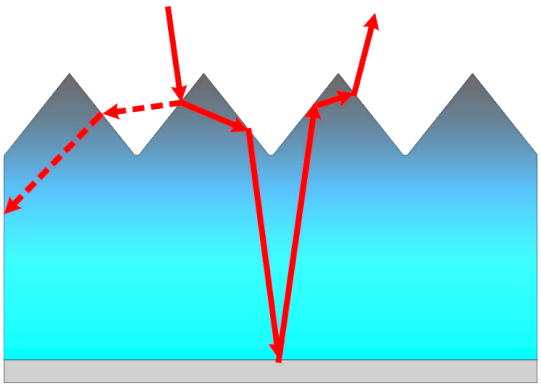

Figure 2.2: Reflection minimizing and light trapping effect of pyramid textured surface [10]

types of structures are generally much larger then the wavelength of light. This allows for easy simulation using the ray trace method. More on this will be explained in section 2.2.

An interesting phenomenon occurs if the surface structure size is reduced to or below the wavelength of light incident on the surface. Namely, reflections are almost entirely eliminated. These structures have been given the name sub-wavelength structures (SWS). First observed in nature on the surface of moth eyes, these structures can reduce reflection values below 0.1% for visible light; effectively making the moths invisible to predators at night [5]. This effect is due to the specific size, shape, and period of the SWS located on the moth eyes. When light falls upon a SWS the effective refractive index is governed by the ratio between the ridges and channels as described by the effective medium theory (EMT) [12]. By adjusting the shape of the SWS, a gradient index of refraction is created, as can be seen in figure 2.3, and reflections are almost entirely eliminated. This can be understood by adjusting equation 2.1. As n_2 approaches the value of n_1 the numerator reduces and total reflectance approaches zero. Not only do they produce minimal reflections, SWS are able to preform better than ARC even at large angles of incidence [5]. Additionally, the diffraction of light into large angles creates a larger optical path through the absorbing layer. This effect is especially useful for thin-film solar cells [13].

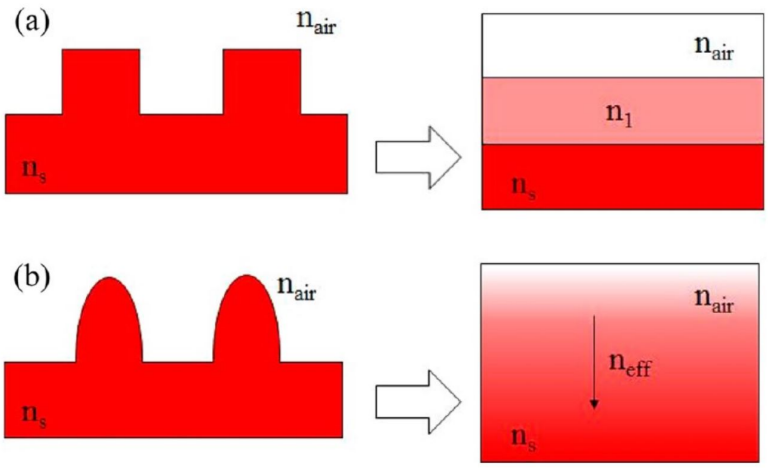

Figure 2.3: Analogy between SWS and respective index of refraction: (a) with ridged structure and (b) with parabolic structures thereby forming gradient index. [5]

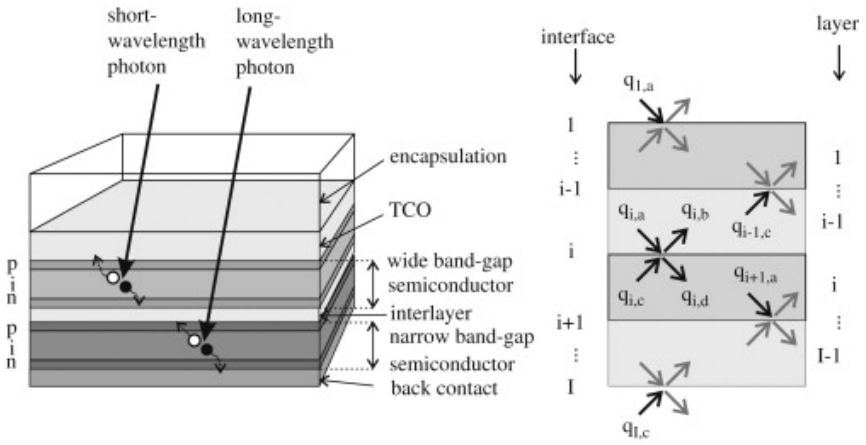

Figure 2.4: Schematic of multijunction solar cell (Left) modeled by net radiation method (Right) [14]

Unfortunately, this is an oversimplification of how these structures interact with light. Due to the complex relation between SWS size and wavelength, the EMT can lead to inaccuracies when simulating complex structures. Therefore, a more comprehensive understanding of how SWS interact with light can be gathered through the use of wave optics.

2.2. GenPro4

As previously mentioned, GenPro4 is aimed at providing a quick and accurate way of modeling optical effects within a solar cell. This software can be used to gather useful information about reflection and absorption losses by a variety of materials, cell structures, and AR techniques. Additionally, the ability to determine absorption per cell layer, allows GenPro4 to quickly current match different layers in a multijunction solar cell [4].

This model is built upon the net radiation method as first formulated by Siegel [15]. As the name implies, net transmittance and reflectance are calculated at every interface. This produces the set of four linear equation at every interface as given in equation 2.5.

$$\begin{cases} q_{ia} = \tau_{(i-1)} q_{(i-1)d} \\ q_{ib} = r_i q_{ia} + t_i q_{ic} \\ q_{ic} = \tau_i q_{(i+1)b} \\ q_{id} = r_i q_{ic} + t_i q_{ia} \end{cases} \tag{2.5}$$

With r_i the reflection for interface i, transmittance at the same interface $t_i = 1 - r_i$, and τ_i the transmittance through layer i calculated using the absorption coefficient of the material [14]. A schematic of the net radiation method can be seen in figure 2.4.

The net radiation method as described above is limited to flat interfaces [14]. As explained in previous sections, flat interfaces generates undesirable reflection values. Therefore, this model needs to be adapted to allow for the implementation of textures surface like the ones described in section 2.1.2. To achieve this, the reflection and transmittance per angle of incidence needs to be calculated. The values in equation 2.5 then become matrices with every element in the matrix representing a reflection or transmittance probability for a given angle of incidence. This generates four matrices ($\mathbf{r}_i^+$,$\mathbf{t}_i^+$,$\mathbf{r}_i^-$,$\mathbf{t}_i^-$) known as scatter matrices for every

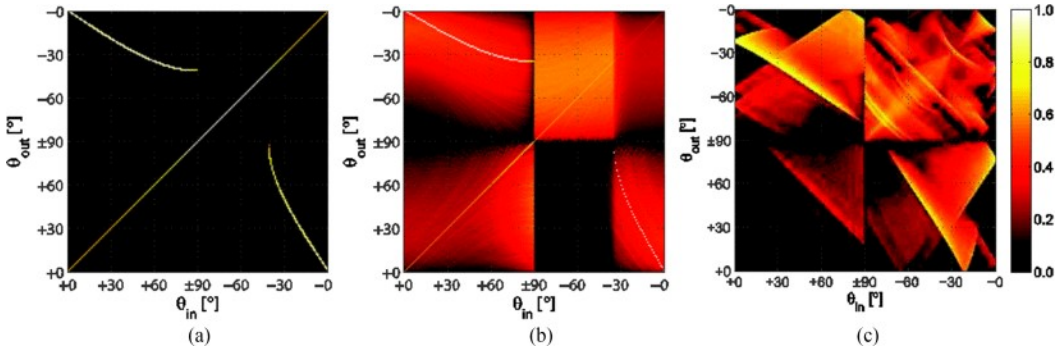

Figure 2.5: Scatter matrices for three different interfaces: flat (a), nanotextured (b), and micro-textured (c). Plots (a) and (c) are modeled using the GenPro4 ray tracer, whereas plot (b) is modeled using the scalar scatter theory. [4]

interface i. These four matrices can be placed in a 2×2 array for visualization, as can be seen in figure 2.5. Generating these scattering matrices can often be computationally intensive for complex surface tinctures. GenPro4 has implemented two methods to do this: ray and wave optics models.

When light interacts with a micro-textured surface (larger than it's wavelength), the scattering can be described by simple ray optics [4]. GenPro4 has an integrated ray tracer that forms a scatter matrix by determining reflection and transmittance angles for every angle of incidence. A plot of the scattering matrix for a pyramid textures glass surface can be seen in figure 2.5c. The figure shows a large angle distribution for every angle of incidence. Each column has a unit sum, thus demonstrating the conversion of energy. Additionally, symmetry can be seen along the diagonal. This is expected and also a requirement as per the reciprocity theory of optics, also known as Helmholtz reciprocal principle. Light from point A to B will follow the same path and with the same magnitude if traveled in the reverse direction [4, 16]. These two key properties can also be seen in figure 2.5a, light incident on a flat glass surface.

GenPro4 also incorporates a wave optics model developed by Jäger [6] based on the scalar scattering model (SSM). A brief overview of this model and it's limitations will be given in the following section 2.2.1

2.2.1. Scalar Scattering Wave Model

As previously mentioned, simulating SWS requires the solving of Maxwell's equations. Often times this can lead to incredibly long computational times or a very limited scope of simulation due to the computational complexity of this task. The scalar scattering model (SSM) developed by Jäger [6] allows for the quick computation of large solar cell areas. Unfortunately, this model does have a few limitations.

In figure 2.5(b), a smearing effect of the spectral reflection (figure 2.5(a)) can be observed. This is due to the diffracting effect of SWS. Each point in the interface is simulated as a point source for a scalar wave but with a phase shift dependent on the height of the SWS [4]. This phase shift assumption can be inaccurate if large textures are used. The emitted scalar waves interact either constructively or destructively to create the scatter matrix seen in the figure. Similar to the other two plots, every column adds up to 1 and thus energy is conserved. However, the scatter matrix generated from the scalar scattering model does not follow the reciprocity theory as is required for all optical interfaces.

The scalar scattering model assumes the total reflectance and transmittance of a textured surface can be modeled by a flat surface, however, at large incident angles and large structures this assumption is incorrect [17]. This assumption also accounts for the large black spot in the scatter matrix, figure 2.5(b). Here, light travels form a material with higher refractive index to one with lower refractive index (i.e. light traveling from the bottom of the cell to the top). At roughly -30 degrees and below, all incident light is reflected back into the incident medium, also known as total internal reflection.This is clearly not correct as we always expect a portion of light to be transmitted by SWS due to their diffractive effect [5, 9].

Due to the possible errors the scalar scatter model can produce, care needs to be taken when implemented. Alternative, rigorous, wave optics models have been developed and validated by several research groups. Several models will be discussed in the following section.

2.3. Alternative Wave Models

As mentioned by Santbergen et al. [4], GenPro4 is able to incorporate many different models for textures surfaces. The only requirement is that these models give an angular distribution of reflectance and transmittance at every angle of incidence in the form of a scatter matrix. In this section a brief overview will be given of several alternative wave optics models. Following this a decision will be made on which model will be further developed and implemented into the new optical solar cell simulation.

2.3.1. Transfer Matrix Method

The transfer matrix method (TMM) is a fast and simple method able to calculate reflectance and transmittance at multiple wavelengths and angle of incidence [18].This is done by slicing the ARC into homogeneous layers at which reflectance, transmittance, and absorbance can be calculated. To determine the properties of each layer, often times the effective medium theory is used. As previously explained, this translates the ARC into a effective medium with a constant, homogeneous, refractive index. In figure 2.6 demonstrates the theory behind the TMM. For thin coherent layers, such as the thin ARC seen in figure 2.6, the TMM is often used, as is also the case within GenPro4. Unfortunately, the inability to simulate complex structures [18] as well as the generalization due to the use of the EMT prevents from using this method to simulate SWS.

2.3.2. Rigorous Coupled Wave Analysis

Also known as the Fourier modal method, rigorous coupled wave analysis (RCWA) is a semi-analytical method originally developed to simulate wave guides. Similar to the TMM, RCWA slices the AR structure into numerous sublayers to create a simplified structure. However, unlike TMM, RCWA only creates homogeneous layers in the direction of propagation (Z axis) and can therefore handle any morphology in the other two directions (X-Y axis) [18]. Throughout each sublayer, the wave propagation can be calculated. At the interface between sublayers, boundary conditions need to be matched. This is achieve by solving Maxwell's curl equations in the Fourier domain. To correctly model any arbitrary structure, an infinite number of Fourier modes is needed. By truncating the Fourier modes a finite and computationally solvable method arises.

By increasing the number of sublayers, the shape of the SWS can better be approximated, as can be seen in figure 2.7. The exact number of layers needed is dependant on the shape of the

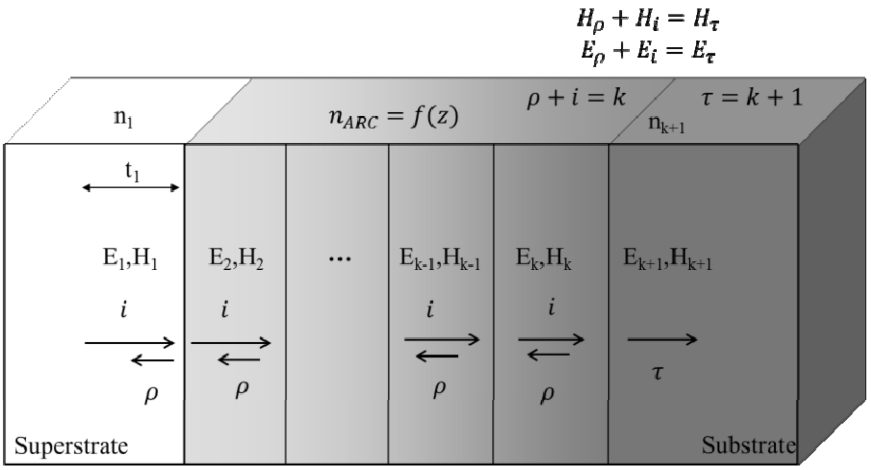

Figure 2.6: TMM being implemented for a ARC by slicing it into k-1 layers [7]

structure, with steeper structures needing less layers and vice versa. Additionally, the number of diffraction modes needed for an accurate simulation is difficult to determine beforehand, as this is dependent on numerous factors such as: size, shape, and refractive index of the structure. Fortunately, solar cells make use of dielectric materials with low refractive indices. This allows the number of Fourier modes to be truncated significantly, allowing simulations to be completed in just a few seconds [8].

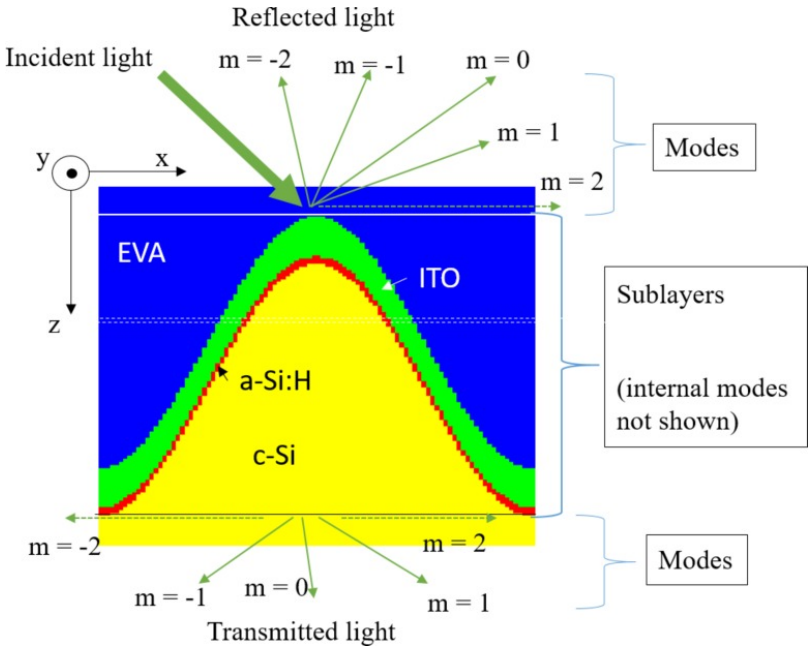

Figure 2.7: Visualization of RCWA subdivision of SWS with 100 sublayers and 3 diffraction modes [19]

Although this method was first implemented for wave guide analysis, RCWA has proven to be a useful tool in the development of SWS. Numerous research groups have proven the usefulness of this robust and fast simulation method [8, 18–20]. The uncertainty on this method lies in the need for periodic structures. Sub-wavelength structures can be developed to be periodic, however, for the solar cell application a low reflection value is desired over a large range of wavelength and incident angles. As Kuo et al. [5] proved, random textured SWS have the best

performance in this case. Thus a limitation of this method is evident: random SWS can not be simulated accurately. However, Lokar et al. [19], Lehr et al. [21], and Agrawal and Frei [22] have all developed novel approaches to overcome this limitation through the use of large unit cells with a pseudo-periodic geometry.

2.3.3. Finite Difference Time Domain

Finite difference time domain(FDTD) is a well known and widely used rigorous simulation method. It's robust nature comes from the discritization of any material, device, or structure via the Yee cell, first introduced by Yee in 1966 [7]. By spacially discretizing the simulation domain into cubes, Yee was able to solve any EM model by offsetting Maxwell electric and magnetic components as can be seen in figure 2.8. This allows one point to be calculated and used as input for the neighboring cells. In this way the FDTD steps through the cell structure and calculates the field strength at every point for every time step. Once all cells have been updated the next time step can be simulated. Given enough grid points and computational power any structure can be modeled in this way.

The finite difference time domain method is often used as an alternative to RCWA as it is more robust for complex aperiodic structures. For periodic dielectric structures this method is slower. For steep oblique incidence, > 70 degrees, simulation time increases greatly as the propagation speed through the device becomes slower. However, unlike RCWA, the electric and magnetic field strength at every point in the structure is directly given as output [7]. This can give added insight into the SWS effects and therefore has been proven useful in structure optimization [7, 23].

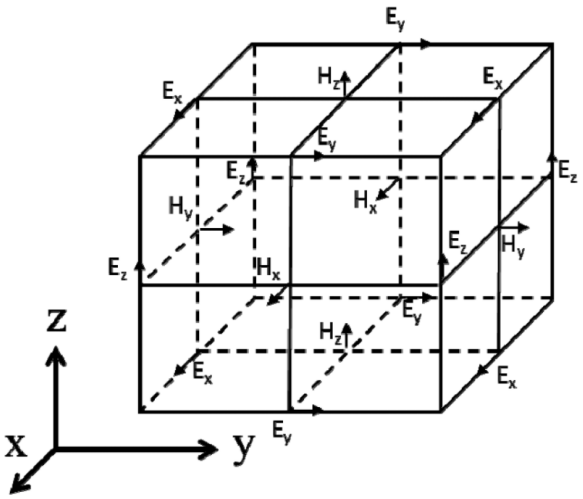

Figure 2.8: Spacily discretization of free space through the Yee cell [7]

FDTD is a very simple, yet powerful, simulation method. Due to the number of sequential calculations needed for this method it benefits greatly from using simple computer languages, such as C++. Generally, such low-level languages are less user friendly, however, several open source FDTD tools have been developed and are available online, such as MEEP [24] and OpenEMS [25].

2.3.4. Finite Element Method

Lastly, the finite element method (FEM) is widely accepted as being the most accurate and computationally expensive Maxwell solver. This is due to the complex and crucial meshing procedure. The generated mesh can conform much closer to the actual structure morphology than the stair step methods used in RCWA and FDTD [7]. Additionally, infinitely complex and anisotropic structures can be simulated with, of course, computational time as trade off. Commercial software is often used for this method as they generally have an optimized meshing algorithm that exceeds in-house performance. Similar to the FDTD, FEM gives the full field strength at every point as output and is often used for final verification of other models.

2.3.5. Compatibility

As this decision criteria is less straightforward than the other two, a short discussion will be held here. Methods such as RCWA and TMM require the solving of eigenvalue problems. High level programs such as MATLAB and Python are well suited for this task. As GenPro4 is already implemented using MATLAB, these models can seamlessly be added to the existing GenPro4 code. Contrarily, FEM and FDTD both require external programs for optimal use. These programs, especially commercial programs, are very powerful but not always user friendly; leading to steep learning curves. Additionally, FEM and FDTD both require post processing as the outputs need to be adapted to integrate with GenPro4. These factors lead to increased user complexity as, generally, more steps need to be taken to utilize these programs.

2.4. Conclusion

GenPro4 aims to model the optical effects within a solar cell in a simple user friendly, yet accurate way. The current wave optics model, scalar scatter model, has accuracy issues as were clearly seen when plotting the scatter matrix of a SWS. Therefore an alternative model was sought. A brief overview of several wave optics models have been presented, each with its benefits and drawbacks. Throughout this research a clear trade off can be seen: accuracy for computational complexity. This fact makes an optimal model difficult to choose. The computational power of computers has increased significantly since several papers referenced in this introduction have been written. Methods such as FDTD weren't even solvable on the nanometer scale when they were first developed as the computer memory needed far exceeded what was then the norm. Increases in computer resources, namely computer RAM, would benefit all methods mentioned. Nonetheless, a method needs to be chosen and an overview of the alternative models with respect to our decision criteria is given in the table below.

Table 2.1: Summery of optical model decision criteria

Features	TMM	RCWA	FDTD	FEM
Accuracy	-	-/+	-/+	+
Compatibility	+	+	-/+	-/+
Speed	+	+	-/+	-

As previously mentioned our criteria were as followings: speed, accuracy, and compatibility. Due to accuracy issues TMM is completely eliminated as option. With respect to speed, RCWA is the winner but this advantage quickly disappears for more complex structures. Compatibility also favors RCWA as it can easily be implemented using MATLAB, the language which Gen-

Pro4 is implemented in [4]. Similarly to the SSM, RCWA can be implemented without further user input, allowing the user to easily switching between models within GenPro4. Therefore, RCWA will be implemented and incorporated into GenPro4. Additionally, a few features will be added to the standard RCWA as will be further explained in the following chapter.

3

RCWA

RCWA is considered a semi-analytical method of solving Maxwell's equations in the Fourier domain. Through the slicing of a complex structure into several layers, a simplification of the partical differential equations can be made, thus allowing for the quick and efficient simulation of these structures. Often times the longitudinal directions (x, y) are solved numerically and the transverse direction (z) analytically, thus being semi-analytical. Although a stable implementation of RCWA has been published in 1995 by Moharam et al. [26], further improvement has been published in the recent year by authors such as Auer [27] and Rumpf [28].

In this chapter a basic explanation of RCWA will be given based on formulation given by Auer [27] as well as some adaptations needed to incorporate this method into GenPro4. Namely, a fast and memory efficient implementation of the S-matrix formulation of RCWA developed by Rumpf [28], as well as the angle intensity distribution of the reflected and transmitted fields. Lastly, a method of calculating the internal E-field will be demonstrated.

3.1. Standard RCWA

We start with the time-harmonic Maxwell curl equations

$$\nabla \times \vec{E} = k_0 \mu_r \vec{\tilde{H}} \tag{3.1}$$

$$\nabla \times \vec{\tilde{H}} = k_0 \epsilon_r \vec{E} \tag{3.2}$$

Where μ_r and ϵ_r are relative permeability and permittivity respectively. Due to $\vec{E}$ and $\vec{H}$ (electric and magnetic field) having greatly different orders of magnitude problems may arise with numerical accuracy. To overcome this issue $\vec{H}$ will be normalized to the same order of magnitude as $\vec{E}$ given a unit amplitude incident wave:

$$\vec{\tilde{H}} = i Z_0 \vec{H} \tag{3.3}$$

Here, Z_0 is the impedance of free space given by $\sqrt{\frac{\mu_0}{\epsilon_0}}$ and i representing the imaginary number. Equations 3.1 and 3.2 can be further expanded to the six partial differential equations given below:

$$\frac{\partial E_z}{\partial y} - \frac{\partial E_y}{\partial z} = k_0 \mu_r H_x \tag{3.4}$$

$$\frac{\partial E_x}{\partial z} - \frac{\partial E_z}{\partial x} = k_0 \mu_r H_y \tag{3.5}$$

$$\frac{\partial E_y}{\partial x} - \frac{\partial E_x}{\partial y} = k_0 \mu_r H_z \tag{3.6}$$

$$\frac{\partial H_z}{\partial y} - \frac{\partial H_y}{\partial z} = k_0 \epsilon_r E_x \tag{3.7}$$

$$\frac{\partial H_x}{\partial z} - \frac{\partial H_z}{\partial x} = k_0 \epsilon_r E_y \tag{3.8}$$

$$\frac{\partial H_y}{\partial x} - \frac{\partial H_x}{\partial y} = k_0 \epsilon_r E_z \tag{3.9}$$

By solving for E_z and H_z in equations 3.6 and 3.9, substitution into the remaining four equations can be made. The first equation will become

$$-\frac{\partial E_y}{\partial z} + \frac{\partial}{\partial y}\frac{1}{k_0 \epsilon_r}\left(\frac{\partial H_y}{\partial x} - \frac{\partial H_x}{\partial y}\right) = k_0 \mu_r H_x \tag{3.10}$$

Similar equations can be formulated for E_x, E_y, and H_y.

As previously stated, RCWA takes place in the Fourier domain. However, to translate the given Maxwell's equations to the Fourier domain we need to focus our simulation domain to a single unit cell within our structure. The Fourier transfer of this unit cell will effectively transform our device to infinitely repeating unit cells in the x and y direction, as can be seen in figure 3.1. Due to the periodicity of the system, a Fourier transform can be taken of the remaining four Maxwell equations. To further simplify the formulation can be written in matrix form as given below:

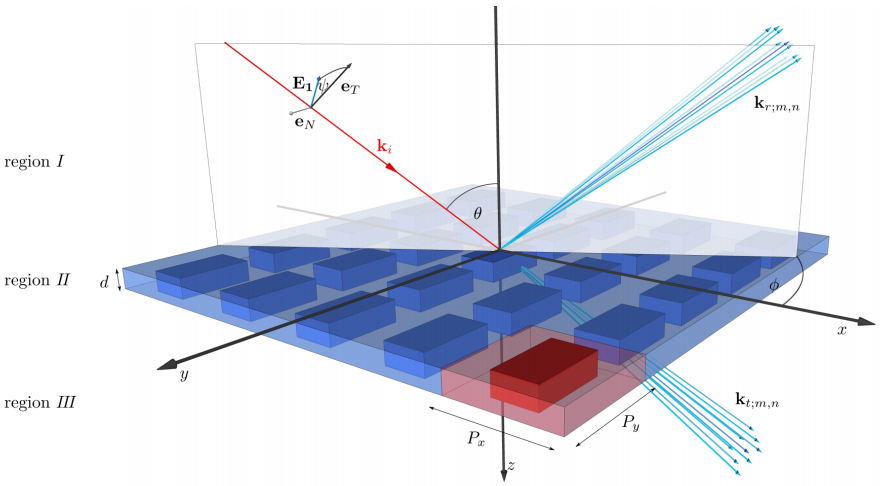

Figure 3.1: Simulation domain as seen in RCWA , with a single unit cell wiht period P_x and P_y given in red [27] The incident wave, represented by the k vector $\mathbf{K}_i$, is being reflected and transmitted, represented by the conical diffracted k vectors $\mathbf{k}_{r;m,n}$ and $\mathbf{k}_{t;m,n}$ respectively.

$$\frac{\partial}{\partial z}\begin{pmatrix} e_x \\ e_y \end{pmatrix} = k_0 P \begin{pmatrix} h_x \\ h_y \end{pmatrix} \tag{3.11}$$

$$\frac{\partial}{\partial z}\begin{pmatrix} h_x \\ h_y \end{pmatrix} = k_0 Q \begin{pmatrix} e_x \\ e_y \end{pmatrix} \tag{3.12}$$

$$P = \begin{bmatrix} K_x[\epsilon]^{-1}K_y & [\mu] - K_x[\epsilon]^{-1}K_x \\ -[\mu] + K_y[\epsilon]^{-1}K_y & -K_y[\epsilon]^{-1}K_x \end{bmatrix} \tag{3.13}$$

$$Q = \begin{bmatrix} K_x[\mu]^{-1}K_y & [\epsilon] - K_x[\mu]^{-1}K_x \\ -[\epsilon] + K_y[\mu]^{-1}K_y & -K_y[\mu]^{-1}K_x \end{bmatrix} \tag{3.14}$$

Equation 3.11 and 3.12 represent the matrix formulations of the first four partial differentials (euations 3.4,3.5,3.7,3.8). With $[\mu]$ and $[\epsilon]$ correspond to the truncated Fourier expansion of a layers relative permeability and permitivity respectively. Additional information will be given in following section 3.2. Matrices K_x and K_y correspond to all possible wave modes along these directions, as formulated in section A.2. Lastly, e_x, e_y,h_x, and h_y now represent the amplitudes of the spacial harmonics in Fourier space. Although equations 3.13 and 3.14 can directly be used to solve for the systems electric and magnetic field solutions, one additional substitution can be made to further reduce the computational complexity of this system. By inserting equation 3.14 into equation 3.13 and normalizing the z coordinate $\hat{z} = k_0 z$ the final differential equation becomes

$$\frac{\partial^2}{\partial \hat{z}^2}\begin{pmatrix} e_x \\ e_y \end{pmatrix} = PQ \begin{pmatrix} e_x \\ e_y \end{pmatrix} \tag{3.15}$$

$$\frac{\partial^2}{\partial \hat{z}^2}\begin{pmatrix} e_x \\ e_y \end{pmatrix} - \Omega^2 \begin{pmatrix} e_x \\ e_y \end{pmatrix} = 0 \tag{3.16}$$

$$\Omega^2 = PQ \tag{3.17}$$

By re-normalizing z the given equation becomes dimensionless. From here we can calculate the eigenvectors $\mathbf{W}$ and eigenvalues $\boldsymbol{\lambda}^2$ of Ω^2. This describes the eigenmodes of the electric field throughout a single layer. The eigenvalues of a matrix PQ are equivalent to the values from matrix QP. Thus, the eigenvectors of the magnetic field can be calculated by using those of the electric field, given by equation 3.19. This leads us to the general field solution

$$\psi(\hat{z}) = \begin{pmatrix} e_x(\hat{z}) \\ e_y(\hat{z}) \\ h_x(\hat{z}) \\ h_y(\hat{z}) \end{pmatrix} = \begin{pmatrix} \mathbf{W} & \mathbf{W} \\ -\mathbf{V} & \mathbf{V} \end{pmatrix} \begin{pmatrix} e^{-\boldsymbol{\lambda}\hat{z}} & 0 \\ 0 & e^{\boldsymbol{\lambda}\hat{z}} \end{pmatrix} \begin{pmatrix} \mathbf{C_f} \\ \mathbf{C_b} \end{pmatrix} \tag{3.18}$$

$$\mathbf{V} = Q\mathbf{W}\boldsymbol{\lambda}^{-1} \tag{3.19}$$

Where the terms $e^{-\boldsymbol{\lambda}\hat{z}}$ and $e^{\boldsymbol{\lambda}\hat{z}}$ represent the forward and backward propagating waves throughout the layer. The coefficients C_f and C_b describe the amplitudes of every eigenmode in the forward and backward directions.

It is worth noting that the eigenvalue problem as stated in equation 3.16 is not always valid. Namely, when the period is an integer multiple of the wavelength the determinate of matrix PQ becomes zero. This lead to a zero solution and thus is not a valid eigenvalue problem. To overcome this problem a slightly different wavelength needs to be used. For example, a structure with period 900 nm will lead to computational errors at wavelengths of 450 and 900 nm. A small step of 1 nm is enough to produce a valid output. As this issue is know before simulation, these wavelength values can be adjusted beforehand.

We now have a generalized, dimensionless, normalized solution for both the electric and magnetic fields within a layer in our solar cell. To fully simulate a nanostructure we need to solve this eigenvalue problem for every layer in our device. A computationally efficient and mathematically stable way of doing this is through the use of S-matrices. The use of S-matrices will be further explained in the section 3.3.1.

3.2. Permittivity and Permeability Truncation

RCWA approximates the textured surface in terms of spacial harmonics by Fourier series expansion. Similar to all previous steps, the z component of the permittivity is not taken into account and thus the Fourier series becomes:

$$\epsilon(x,y) = \sum_n \sum_m \epsilon_{nm} e^{in\frac{2\pi}{P_x}x} e^{im\frac{2\pi}{P_y}y} \tag{3.20}$$

This is equivalent to taking the fast Fourier transfer (FFT) of the permittivity. Again, m and n (Fourier modes in x and y direction) need to truncated due to the inability to simulate infinite systems. This will be achieved by truncating m to p and n to q. However, it is important to realize that by limiting the Fourier components we effectively lose resolution in real space. To ensure equal resolution in both direction (x and y) we need to fix the relationship between period and number of Fourier modes

$$\frac{P_x}{p} = \frac{P_y}{q} \tag{3.21}$$

In some cases (e.g. $P_x << P_y$) this can lead to the conclusion that only a few Fourier modes are needed. This can lead to incorrect simulations because p and q also determine the number of wave modes we simulate in each direction. The use of similar number of Fourier components is necessary because ϵ is convolved over every wave mode as seen in equation 3.13 and 3.14.

This convolution is performed via the 2D Toeliptz matrix $[\epsilon]$ with all diagonal values being equivalent.

$$[\epsilon] = \begin{bmatrix} \epsilon_0 & \epsilon_1 & \epsilon_2 & \dots & \epsilon_{pq} \\ \epsilon_{-1} & \epsilon_0 & \epsilon_1 & \epsilon_2 & \dots \\ \epsilon_{-2} & \epsilon_{-1} & \epsilon_0 & \epsilon_1 & \epsilon_2 \\ \dots & \epsilon_{-2} & \epsilon_{-1} & \epsilon_0 & \epsilon_1 \\ \epsilon_{-pq} & \dots & \epsilon_{-2} & \epsilon_{-1} & \epsilon_0 \end{bmatrix} \tag{3.22}$$

A similar matrix can be generated for the relative permeability. However, almost all solar cell materials are non-magnetic, thus leading to a homogeneous unitary permeability [27]. If a Fourier transfer were to be taken from such a material all values would be zero except for the zero order mode, ϵ_0 in equation 3.22 . To save computational time we can therefore create a identity matrix of size $pq \times pq$ donated by $[\mu]$.

3.2.1. Gibbs Phenomenon

As seen in the previous section, the surface of our device is translated to the frequency domain via a combination of Fourier modes. Due to the truncation of the Fourier transfer, jumps in permittivity at boundaries can lead to significant errors. This can lead to over or under estimates at boundaries even if an infinite number of modes were to be used, this is known as the Gibbs phenomenon. Unit cell complexity can also increase the effect of the Gibbs phenomenon. A simple binary structure, such as the one seen in figure 3.2, can often be modeled by just a few modes [1]. Increasing the unit cell complexity would require the use of an increased number of Fourier modes. This leads to runaway computational time as the eigenvalue problem that needs to be solved for RCWA grows cubicly with the number of modes.

The use of Fourier series to approximate a surface, theoretically limits RCWA to only being able to model periodic interfaces. However, quasi periodic structures may still be able to be modeled with RCWA through the use of large unit cells. Again, larger unit cells require more Fourier modes to be used to model the cell accurately. Exactly how many modes needs to be used is not easily determined ahead of time. Therefore, a convergence analysis needs to be done to determine the accuracy of the simulation. If an inadequate number of modes are used, the surface will not be represented correctly, but this will not be observed at the output. The simulation will appear correct as energy will always be conserved. Thus care needs to be taken with complex structures, and several simulations need to be done with a varying number of modes.

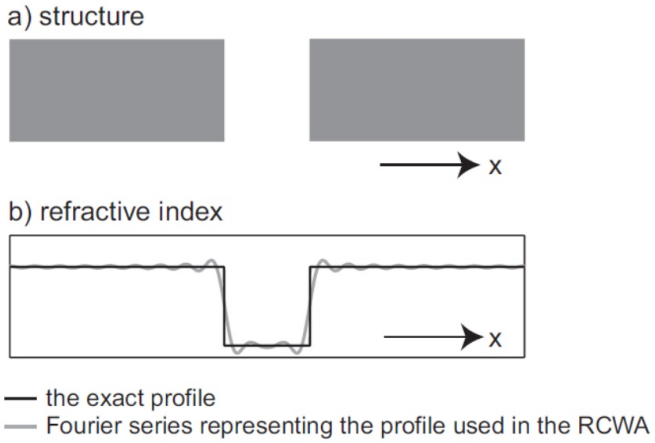

Figure 3.2: The Gibbs phenomenon is observed at the boundaries between two materials with different relative permittivity as can be seen in the lower figure [29]

[1] Given that the relative permittivity difference is not too large (e.g. 1 -> 1.5)

3.3. Improvements Made to Standard RCWA

In this section we will present a few improvements and added features that were chosen to allow for better integration or more accurate results. We start with the S-matrix formulation, based on the work of Rumpf [28], which simplifies the computations and allows for a much more memory efficient simulations. Next, we introduce the an angle intensity distribution which allows RCWA to match it's outputs with GenPro4. Lastly, we incorporate local absorption to determine where in our material the light is absorbed, similar to the method introduced by Brenner [30] and Kim et al. [31].

3.3.1. S-Matrix Formulation

S-matrices, also known as scatter matrices[2], are often used in other area of optics and quantum mechanics as a way of coupling input modes to output modes. Due to the robust nature of their formulation as well as ability to be computed in parallel, the S-matrix formulation of RCWA has gained popularity in the previous years [18, 22, 27].

S-matrices allow for the coupling of input and output waves via a single matrix multiplication. In essence this method allows us to determine the power in each wave mode as it transitions from one layer to the next. A generalized form of the S-matrix equation is given by equation 3.23, and a visual overview can be seen in figure 3.3.

$$\begin{bmatrix} C_1^b \\ C_2^f \end{bmatrix} = \begin{bmatrix} S_{11}^i & S_{12}^i \\ S_{21}^i & S_{22}^i \end{bmatrix} \begin{bmatrix} C_1^f \\ C_2^b \end{bmatrix} \tag{3.23}$$

Here the the mode coefficients C_1^b ,C_2^b ,C_1^f , and C_2^f describe the field just outside the ith layer. The subscript indicate which layer and the superscript indicate the forward and backward propagation direction. The S-matrix values are square matrices that quantify how much energy is transferred into every eigenmode. Any arbitrary input field can be used and the S-matrix for layer i will determine how much energy remains in each mode after the incident field travels through that layer. A full derivation of how these S-matrices are calculated is given in appendix A.

[2]Not to be confused with the scatter matrices used in GenPro4, which represent the angle intensity distribution

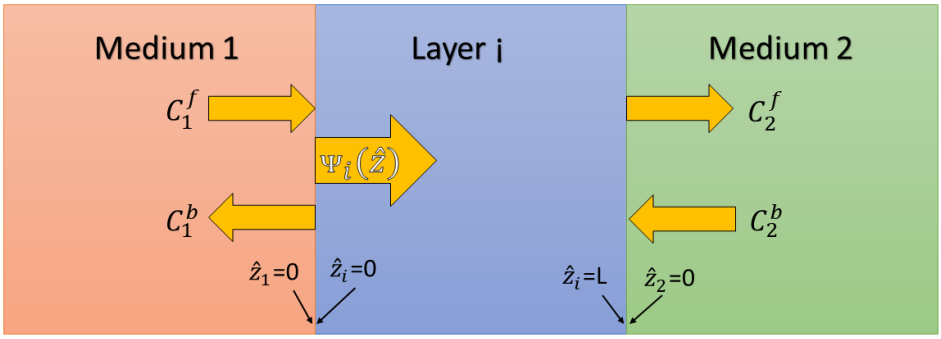

Figure 3.3: The scatter matrix described how much energy is transferred throughout layer i as well as the boundary conditions at interface $\hat{z}_1$ and $\hat{z}_2$

To calculate the S-matrix values we need the material properties and eigenvalues of the current layer as well as the surrounding two layers. Not only does this require solving and storing the eigenvalue problem for every layer to be used in the previous and next layers, it also prevents us from parallelizing the computations. Fortunately, Rumpf [28] has re-formulated the S-matrix approach to overcome these challenges and shown a speed increase of 23% compared to the current formulation as given above.

By surrounding each layer in our device by a zero thickness vacuum layer we can eliminate the need to store, or compute, the two surrounding medium eigenvalue problems. Additionally, by now having a perfectly symmetric system (medium 1 & 2 in figure 3.3 being identical) the scatter matrix calculations are further simplified. Each layer S-matrix can now be computed with a single eigenvalue problem for the current layer i as well as the eigenvalues of free space. These can be calculated beforehand and are used for every layer in our device.

Multiple S-matrices can be combined into a single global matrix through the use of the Redheffer star product [32] as given below

$$\begin{bmatrix} S_{11}^{AB} & S_{12}^{AB} \\ S_{21}^{AB} & S_{22}^{AB} \end{bmatrix} = \begin{bmatrix} S_{11}^{A} & S_{12}^{A} \\ S_{21}^{A} & S_{22}^{A} \end{bmatrix} \otimes \begin{bmatrix} S_{11}^{B} & S_{12}^{B} \\ S_{21}^{B} & S_{22}^{B} \end{bmatrix} \tag{3.24}$$

$$\begin{aligned} S_{11}^{AB} &= S_{11}^{A} + S_{12}^{A}\left[\mathbf{I} - S_{11}^{B}S_{22}^{A}\right]^{-1} S_{11}^{B}S_{21}^{A} \\ S_{12}^{AB} &= S_{12}^{A}\left[\mathbf{I} - S_{11}^{B}S_{22}^{A}\right]^{-1} S_{12}^{B} \\ S_{21}^{AB} &= S_{21}^{B}\left[\mathbf{I} - S_{2}^{A}S_{11}^{B}\right]^{-1} S_{21}^{A} \\ S_{22}^{AB} &= S_{22}^{B} + S_{21}^{B}\left[\mathbf{I} - S_{22}^{A}S_{11}^{B}\right]^{-1} S_{22}^{A}S_{12}^{B} \end{aligned} \tag{3.25}$$

In the case of a multi layer RCWA analysis, S^B would represent the current scatter matrix and S^A would be the previous layer. To be further memory efficient we can generate global scatter

matrix that will be updated after every layer. Then S^A would represent the previous global matrix, S^B the current layer matrix, and S^{AB} the new global scatter matrix.

By updating the global scatter matrix for every layer we have no need to remember all scatter matrices for every separate layer, as these are incorporated into the global matrix. This has the benefit of being much more memory efficient as only two matrices need to be remembered, the current layer matrix and the global scatter matrix. After calculations of all layers has been completed, the reflection and transmitted field can be calculated. To do this we need to create a source plane wave. As we are working the the Fourier domain, this corresponds to a delta function at the zero order mode given by c_{inc}.

The incident light propagates in the forward direction from medium one into the structure. We make the assumption that no light is incident from the opposite direction. This isn't always correct within solar cells. Therefore, the simulation will be run twice to account for light incident from the opposite direction. This is done because the RCWA as formulate here calculates relative power transmitted and reflected. As we don't know the relationship between the relative power reflected back into the structure we can ignore it and re-run the simulation for light incident from the bottom of the cell. This also fits the procedure used by the SSM and other models currently incorporated into GenPro4.

The reflected (c_{ref}) and transmitted (c_{trn}) wave modes can now be calculated via the following relation:

$$\begin{bmatrix} c_{ref} \\ c_{trn} \end{bmatrix} = \begin{bmatrix} S_{11}^{global} & S_{12}^{global} \\ S_{21}^{global} & S_{22}^{global} \end{bmatrix} \begin{bmatrix} c_{inc} \\ 0 \end{bmatrix} \tag{3.26}$$

We can now use the mode coefficients and equation 3.18 to calculate the transmitted and reflected fields

$$\begin{bmatrix} r_x \\ r_y \end{bmatrix} = \mathbf{W}_{ref} c_{ref} \tag{3.27}$$

$$\begin{bmatrix} t_x \\ t_y \end{bmatrix} = \mathbf{W}_{trn} c_{trn} \tag{3.28}$$

Lastly, to determine the overall field solution we need the longitudinal component of the field. This can be done by using Maxwell's divergence equation leading to

$$r_z = -\frac{K_x r_x + K_y r_y}{k_z^{ref}} \tag{3.29}$$

$$t_z = -\frac{K_x t_x + K_y t_y}{k_z^{trn}} \tag{3.30}$$

Now we can calculate the total reflection R_{tot} and transmission T_{tot} power of all wave modes

$$|\vec{r}|^2 = |r_x|^2 + \left|r_y\right|^2 + |r_z|^2 \tag{3.31}$$

$$\mathbf{R} = \frac{Re\left[-k_z^{ref}\right]}{Re\left[k_{inc,z}\right]}|\vec{r}|^2 \tag{3.32}$$

$$R_{tot} = \sum \mathbf{R}(p,q) \tag{3.33}$$

$$\left|\vec{t}\right|^2 = |t_x|^2 + \left|t_y\right|^2 + |t_z|^2 \tag{3.34}$$

$$\mathbf{T} = \frac{Re\left[k_z^{trn}\right]}{Re\left[k_{trn,z}\right]}\left|\vec{t}\right|^2 \tag{3.35}$$

$$T_{tot} = \sum \mathbf{T}(p,q) \tag{3.36}$$

3.3.2. Angular Intensity Distribution

To incorporate RCWA in to GenPro4 the angular intensity distribution (AID) is needed as this is used in the net radiation method as mentioned in section 2.2. Given that RCWA is a Fourier method, the solution to the diffraction problem takes place on the flat k-space as can be seen in figure 3.4.

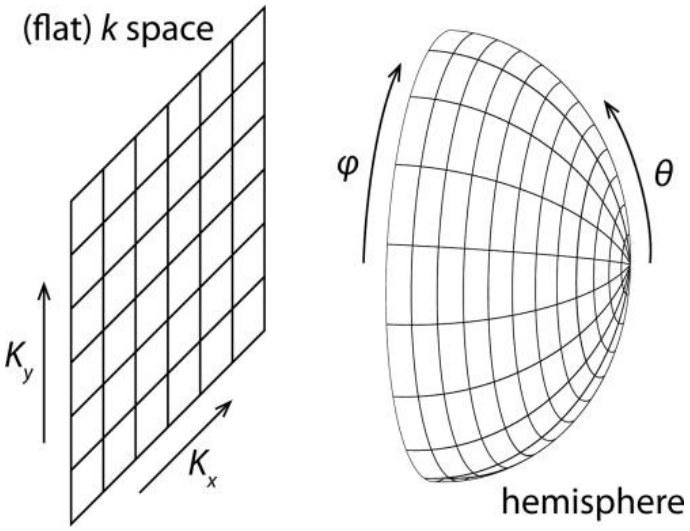

Figure 3.4: Coordinate transfer from curved spherical coordinates to the flat k-space [6]

We can make use of the coordinate transform between k-space and the spherical coordinates (ϕ,θ) to determine the direction of each wave.

$$K_x = k_0 n_{1,2} sin\theta cos\phi \tag{3.37}$$

$$K_y = k_0 n_{1,2} sin\theta sin\phi \tag{3.38}$$

We can now relate every point on k-space to a combination of angles (ϕ,θ), however, GenPro4 only makes use of the inclination angle θ. This simplification is due to the isotropic nature of solar cell materials, thus allowing the AID to be independent of ϕ. We can therefore average over all azimuth angles (ϕ) and simplify the coordinate transfer to

$$K_x^2 + K_y^2 = k_0^2 n_{1,2}^2 sin^2\theta \tag{3.39}$$

This method is similar to that used by Jäger [6]. We can now use RCWA to determine the power transmitted or reflected in every point in k-space. A simple validation of this model through the simulation of a binary grating is given in section 4.1.1.

3.3.3. Local Absorption

Within solar cells light is absorbed due to the complex index of refraction of the material, also known as the extinction coefficient. RCWA used the law of conversation of energy to determine a global absorption value A_{global}:

$$A_{global} = 1 - R_{tot} - T_{tot} \tag{3.40}$$

Within solar cells many layers are absorbing and may not contribute to the energy produced by the cell. This is often referred to as parasitic absorption. Therefore, a general global absorption as given by equation 3.40 does not give the spacial resolution needed to determine how much light is parasitically absorbed and not. We must therefore determine the local absorption. Brenner [30] has developed a simple and stable method to achieve this. We can calculate the absorbed power P_a per unit volume as given below

$$P_a = \frac{\epsilon_0 \omega}{2} \iiint Im(\epsilon(r))|E(r)|^2 dV \tag{3.41}$$

Here, the product of the complex permittivity and magnitude of the electric field gives us the local absorbed power per unit volume. Given the incident field is of unit amplitude, this equation can be further simplified, thus allowing us to use the relative dimensionless electric field as given by RCWA. Discretizing leads the following summation:

$$P_{rel,a} = \frac{\delta z}{Nx\, Ny} \frac{k_0^2}{k_{inc,z}} \sum_{j=1}^{Nx} \sum_{i=1}^{Ny} \sum_{k=1}^{Nz} Im\left(\epsilon(x_j, y_i, z_k)\right) \left|E_r(x_j, y_i, z_k)\right|^2 \tag{3.42}$$

With Nx,Ny,Nz the total number of points in the x,y, and z directions respectively. The spacial resolution in the z direction is given by δz and the incident wave in the z direction $k_{inc,z}$ (see equation A.8). Lastly, the electric field at every point within our structure is not directly an output given by RCWA, however, this can easily be calculated given the mode coefficients within each layer.

Internal Mode Coefficients

The mode coefficients within each layer describes the power of each wave in both the forward and backward directions, as described in section 3.3.1. In our implementation of RCWA, we make use of S-matrices to couple the mode coefficients of one layer to the two surrounding layers. In this way we can we can use the global scatter matrix to solve for the unknown, external, coefficients c_{ref} and c_{trn} as given in equation 3.26. These values can now be used to solve for the mode coefficients between each layer of our device, similar to the method developed by Kim et al. [31].

The reflected and incident waves, and thus their mode coefficients, remain constant independent on which internal modes we calculate as they are only dependent on the total device scatter matrix $\mathbf{S}_g^N$. To determine the internal modes, we need to solve for the incident and reflected wave modes previous to every layer i, as given in equation 3.44.

$$\begin{bmatrix} c_{ref} \\ c_{trn} \end{bmatrix} = \left[\mathbf{S}_G^N\right] \begin{bmatrix} c_{inc} \\ 0 \end{bmatrix} \tag{3.43}$$

$$\begin{aligned} \begin{bmatrix} c_{ref} \\ c_i^f \end{bmatrix} &= \begin{bmatrix} \mathbf{S}_G^{i-1} \end{bmatrix} \begin{bmatrix} c_{inc} \\ c_i^b \end{bmatrix} \\ c_i^b &= \left(\mathbf{S}_{G(12)}^{i-1}\right)^{-1} \left(c_{ref} - \mathbf{S}_{G(11)}^{i-1} c_{inc}\right) \\ c_i^f &= \mathbf{S}_{G(21)}^{i-1} c_{inc} + \mathbf{S}_{G(22)}^{i-1} c_i^b \end{aligned} \tag{3.44}$$

As previously explained, our device layers are separated by zero thickness free space. The

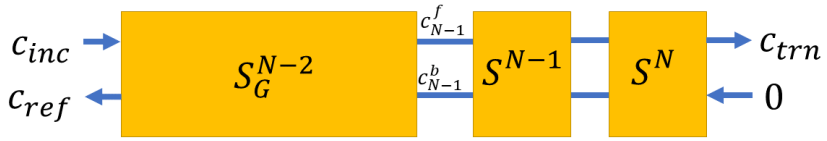

Figure 3.5: The global scatter matrix for layer $N-2$ is used to calculate the wave mode coefficients for the layer $N-1$

mode coefficients as currently given are within the free space gap medium. We can use equation A.1 to solve for the mode coefficients directly within the layer i at $\hat{z} = 0$. Given the mode coefficients we can determine the local E field at every point within our simulation domain. A derivation for this is given in appendix section A.3. For the internal E field calculations we need the eigenmodes, eigenvalues, and eigenvectors per layer. This greatly increases the memory resources needed, and thus will affect the maximum number of Fourier modes that can be calculated.

3.4. Conclusions

We have introduced a basic overview of RCWA as well as a few improvements, such as S-matrix formulation, angle intensity distribution, and the internal mode coefficients needed to determine local absorption. We also discussed the Gibbs phenomenon and how it can lead to inaccuracies within RCWA. For a more thorough explanation of RCWA and its components Auer [27] and Moharam et al. [26] can be referenced. In the following chapter, we will validate our RCWA model and demonstrate the integration with GenPro4.

4

Model Validation and Integration

In this chapter we will validate the RCWA implementation as described in the previous chapter. This will be done through comparing with a simulation of a CIGS solar cell with nano-textures. Additionally, we will demonstrate the fully integrated RCWA model in GenPro. Lastly, a discussion with lessons learned can be found in the final section.

4.1. Nano-textures CIGS Solar Cell

As mentioned in the chapter 2, nano-textured interfaces have been implemented into solar cells to limit the reflection. Within the PVMD group research into solar cells with these types of surface texturing has been conducted. Due to the lack of alternatives, FEM commercial programs have been used to investigate the optical effect of these cell structures. We can use the results from previous research to validate the RCWA model, thus creating a direct comparison between RCWA and FEM.

We will use the FEM results from Rezaei et al. [33]. A simple overview of the cell structure can be seen in figure 4.1. Rezaei et al. optimized layer thickness to maximize current generated in a 750 nm CIGS absorber layer within a solar cell. Above the thick absorber layer, there are several non-conformal layers, from top to bottom: aluminum-doped zinc oxide (AZO), intrinsic zinc oxide (i-ZnO), cadmium sulfide (CdS), and underneath a molybdenum (Mo) back contact. Due to confidentiality, the exact dimensions and thickness of the top layers can not be presented here. However, it can be noted that the period of all interfaces is 330 nm. The metal back contact is an exception to this with smaller texturing with a period of 30 nm.

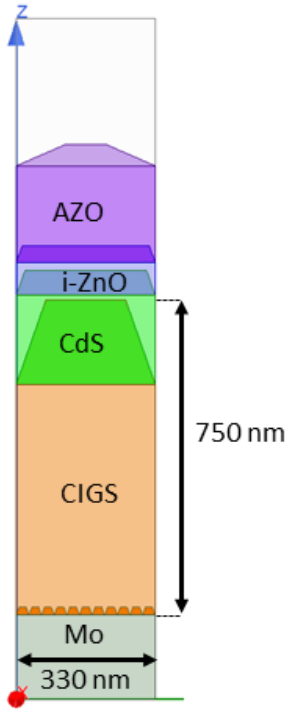

Figure 4.1: Solar cell structure to be simulated with FEM model and RCWA [33]. The exact dimensions of all layers is confidential.

With a period of just 330nm this solar cell makes use of subwavelegth structures for almost the entire AM 1.5 spectrum. To validate the RCWA model we will be modeling the entire structure with only the improved RCWA as presented in chapter 3, thus not yet integrating with GenPro4. This will allows use to determine where differences arise and how they directly correlate to RCWA. All simulations were done on a workstation with 2×6 core Intel® Xeon® (3.47 GHz) CPU with 128 GB of system memory (RAM). An overview of simulation parameters can be seen in the table below:

Fourier Modes	17
Layers	1750
Wavelength Range	350-1100 nm
Resolution x	1 nm
Resolution y	1 nm
Resolution z	0.5 nm

Due to limited time, steps of 50 nm were taken throughout the entire wavelength range. To minimize the effect of the staircase approximation a large number of layers were used, leading to a layer thickness just under 1 nm. All simulations were done with only TE polarized light at normal incidence. The results of all simulations for both RCWA and FEM are given in figure 4.2.

We see very good agreement between the FEM and RCWA model over a large wavelength range. However, at the tail end of the wavelength (> 1000nm) we see clear deviation in both

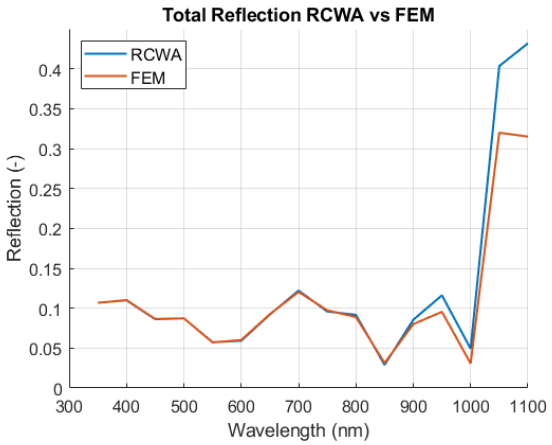

(a) Total Reflection

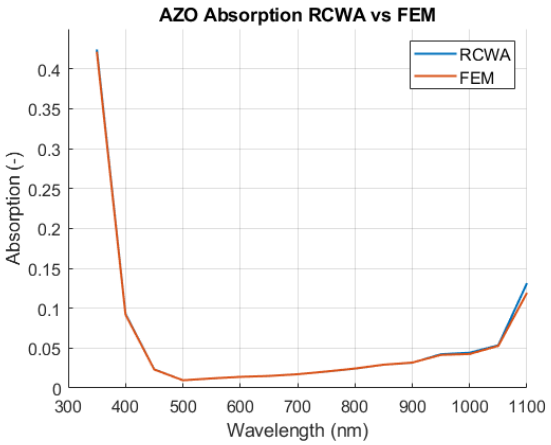

(b) Absorption AZO

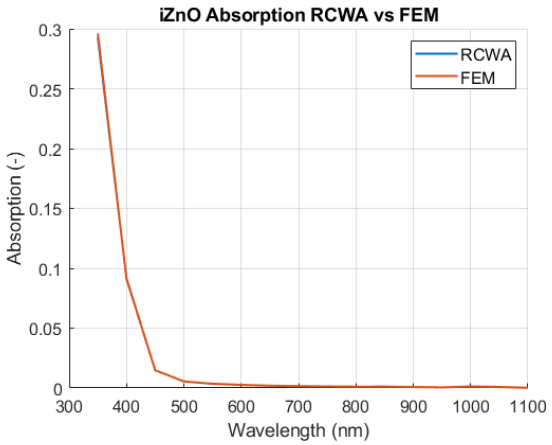

(c) Absorption iZnO

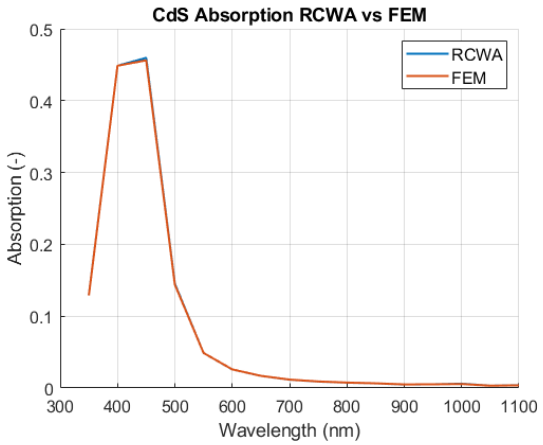

(d) Absorption CdS

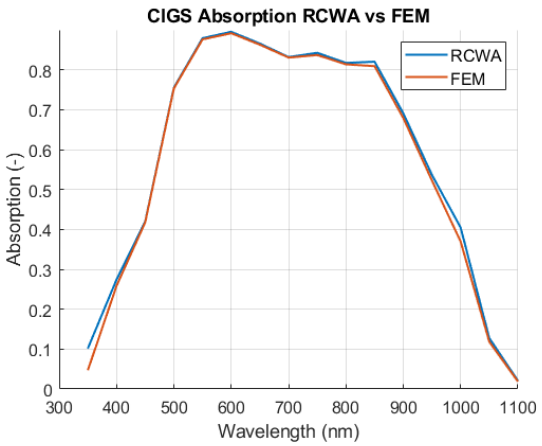

(e) Absorption CIGS

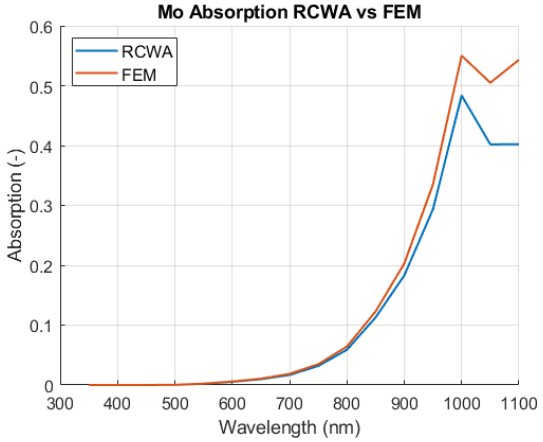

(f) Absorption Mo

Figure 4.2: RCWA vs FEM validation for nano-textured CIGS solar cell

the reflection and molybdenum back reflector absorption values, 37% and 12% difference respectively . This is due to the difficulty of simulating materials with high (complex)refractive index. Generally this mismatch can be solved by increasing the number of Fourier modes. Unfortunately, for metals, this would require a hundred or even several hundred modes, as demonstrated by Fitio et al. [34]. Due to our large simulation domain, this is not possible. Additionally, simulations with this number of Fourier modes would require an extraordinary amount of computer resources, as will be further explained in section 4.2. By not accurately modeling the back metal reflector we observe an increased reflection back into, and out of, the cell (figure 4.2a). This also leads to increased absorption in the other layers as the e-field in these layers is also higher. However, due to these layers having very low extinction coefficients very limited error is observed in the dielectric layers (figures 4.2 b-e).

Lastly, we can also observe a slight divergence at 350 nm in figure 4.2e. Unlike the error at the higher wavelength, this is not due to the inability to correctly model the back reflector with 17 Fourier modes. Evident from the reflection and Mo absorption value (zero due to all light being absorbed) being equivalent to the FEM model. However, these two phenomena are related as they are both solved through the use of additional Fourier modes.

At 350 nm GIGS has an refractive index of $2.35 - i0.724$. Although 17 Fourier modes should be enough to correctly model a material with a index of refraction in this order, instabilities still occur. This is mainly due to the inversion of the s-matrix when calculating the internal mode coefficients, see chapter 3.3.3. If an insufficient number of modes are used, materials with higher complex refractive index can cause instabilities in this step of the calculations, although this is not guaranteed. The simple solution is to increase the number of wave modes:

RCWA 17 modes	0.1016
RCWA 23 modes	0.0476
FEM	0.0470

Table 4.1: GIGS absorption values at 350nm. By increasing the number of Fourier modes used we can increase the accuracy of the RCWA model.

It is also worth noting that this error is also wavelength dependant. By increasing the wavelength the amount of energy found in the higher diffraction modes decreases. This also has the benefit of creating a more stable internal mode calculation. So even though at 400 nm the refractive index increases, to $2.72 - i1.03$, the error with just 17 Fourier modes decreases, as can be seen in figure 4.2e. Here, the GIGS absorption value is 0.274 with the RCWA model and 0.258 with the FEM model.

4.1.1. Scalar Scatter Model vs RCWA

In section 2.2.1 we saw the limitations of the current wave model, scalar scatter model, when modeling a interface with light traveling from an area of high refractive index to an area of low refractive index (see figure 2.5b bottom right quadrant). To demonstrate the ability of RCWA to overcome this drawback we will simulate a binary grating, see figure 4.3.

This structure was chosen as the angle distribution is given by the grating equation

$$n_{trn} sin\theta_{trn} = n_{inc} sin\theta_{inc} + m\frac{\lambda}{P} \tag{4.1}$$

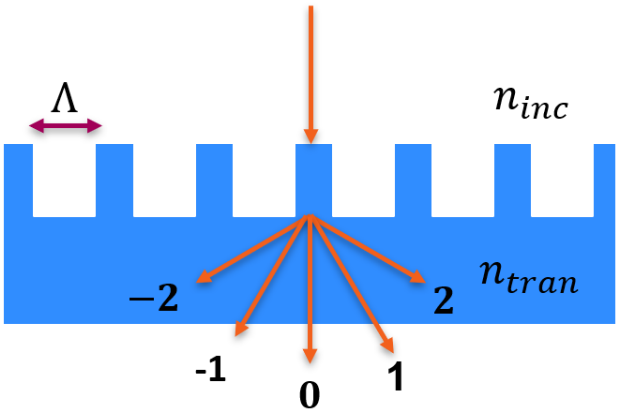

Figure 4.3: Binary grating to be simulated with RCWA and the scalar scatter model. The exact number of diffraction order is not correct for these parameters, but is illustrated to demonstrate the diffraction effect of such a grating.

All values are given in figure 4.4. As we are only interested in the accuracy of the output angles and not necessarily the output power we can use any number of Fourier modes larger then 5 (as this is the minimum umber needed to simulate all allowed wave modes over all angles). The angle distribution as calculated by equation 4.1 can be seen in figure 4.4. Additionally, the scatter matrix from the SSM and RCWA can be found in figure 4.5a and 4.5b respectively, now with logarithmic scale.

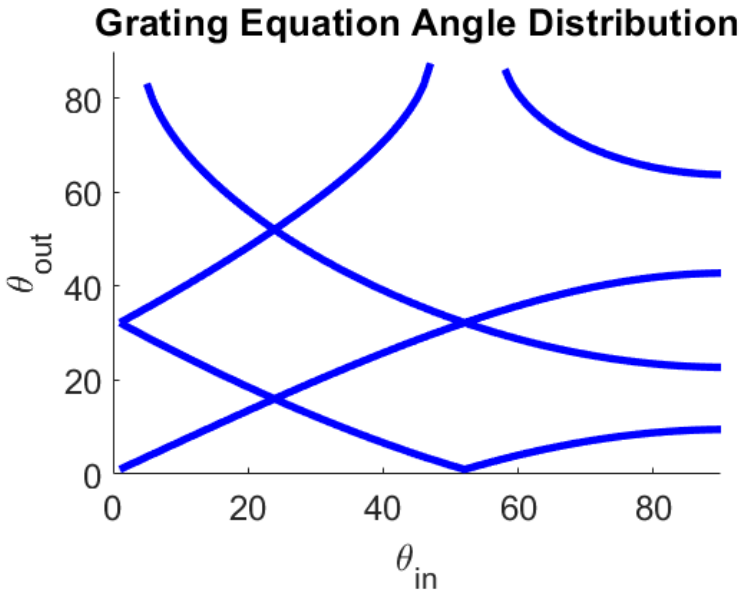

Figure 4.4: Angle distribution as calculated form the grating equation.

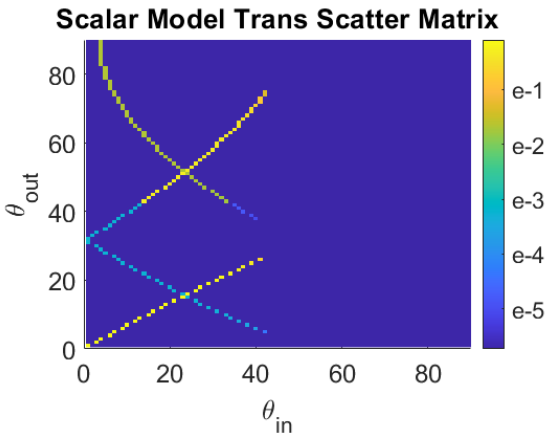

(a) Transmission scatter matrix for binary grating from SSM.

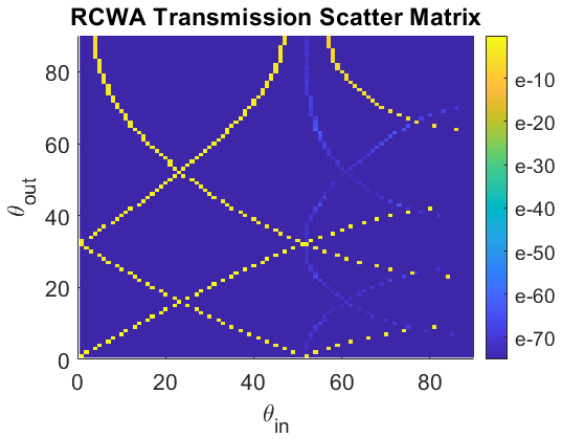

(b) Transmission scatter matrix for binary grating from RCWA.

As we are simulating a two dimensional grating with a three dimensional simulation, we can see an interesting phenomenon in the RCWA scatter matrix, figure 4.5b. We can observe additional very faint blue lines at angles larger than 50 degrees. These lines are not observed in the angle distribution form the grating equations, so they are not excepted. However, as this is a three dimensional simulation, we also simulate the diffraction in all three dimensions. This leads to conical diffraction, despite that not being expected with a two dimensional grating. This has the effect of having slight energy leakage into these allowed diffraction angles. Fortunately, these lines are several orders of magnitude lower than the expected diffraction angles and only become observable with a log plot such as this.

4.1.2. RCWA vs Ray Model

Within GenPro we can choose between three different models to simulate an interface: flat, ray, and wave model. The ray tracer can be used to model flat and large (micro) textured surfaces. The flat model, per definition, can only model flat interfaces and the wave, now RCWA, model can be used for flat and small (nano) textures. Ideally we would like to transition seamlessly from one model to the next, however, it is difficult to determine when these models are valid for the structure they're simulating. To investigate the ability of the wave (RCWA) model to simulate larger textures a periodic sine form structure was investigated with a period of 3 micrometers. For the material ITO was chosen as this has a low index of refraction, thus limiting the number of allowed diffraction modes. The reflection values for this simulation for several Fourier modes and layer numbers are given in table 4.2. Unfortualty, RCWA did not converge for any structures significantly larger than its wavelength. We could try and combat this issue by using a very large number of Fourier modes, however, due to time limitations this was not pursued in this thesis. As modeling 53 Fourier modes requires a simulation time in excess of 16 hours, and computational complexity grows to the fifth order with respect to the number of Fourier modes [19, 27]. Other researchers, did see good agreement between ray tracer and RCWA [19]. This leads us to believe this is possible, at least for specific materials and texture shape.

Table 4.2: Reflection values for sine textured ITO with a period of 3 micrometers and incident wavelength of 900 nm.

Ray model	0.0289
RCWA 43 modes 50 Layers	0.0195
RCWA 43 modes 100 Layers	0.0198
RCWA 53 modes 50 Layers	0.0202

4.1.3. RCWA vs Flat Model

Alternatively, we can decrease the textures surface and compare the results with that of a flat interface. By keeping the aspect ratio (ratio of height to period, 1:4) and wavelength (300 nm) constant, we decreased the period and compared the results to a perfectly flat interface. As expected, with sufficiently small textures the reflection values converge to that of the flat model, see figure 4.6.

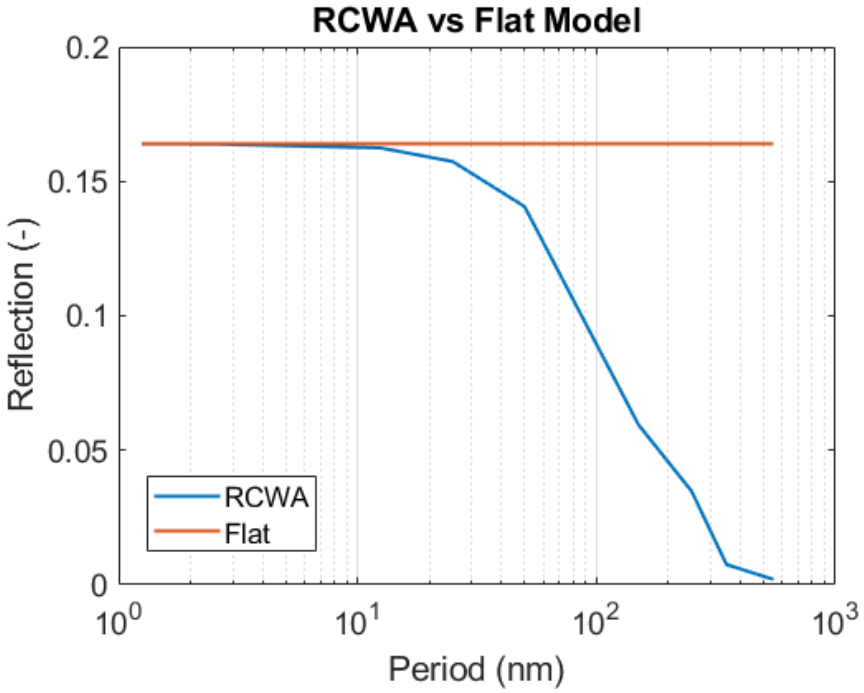

Figure 4.6: By decreasing the texture period we can see an converges with the flat refection values at significantly small period size.

4.2. Discussion

During these simulations a few note worthy things have been discovered and will be discussed here.

Firstly, materials with high absorption are difficult to simulate with RCWA. Due to the large contrast in permittivity at the interfaces in combinations with the higher number of allowed wave modes, highly absorbing materials require a large number of Fourier modes to simulate. Generally, all dielectrics are much more absorbing at the lower wavelengths and less absorbing at higher wavelength. Therefore, when the number of Fourier modes used in the RCWA is not varied we see that the accuracy of our results becomes lower at these high absorbing

wavelength. As was the case for the CIGS simulation at 350 nm, where the inadequate number of Fourier modes resulted in inaccuracies in the local E-field calculations.

A simple solution to this issue would be to do additional sensitivity analysis and vary the number of Fourier modes used per wavelength. This can become very time intensive, thus alternatively a single sensitivity analysis can be done at the lowest wavelength when the dielectric materials are the most absorbing and these parameters can be used throughout the whole simulation.

At longer wavelengths we also observed a deviation from the FEM model. This was due to the inability to accurately model a metal interface with the number of Fourier modes used. Unlike dielectrics, metals are highly absorbing at all wavelengths. To accurately model these materials other researchers have used several hundred Fourier modes [34]. This is neither time efficient nor physically possible with the computer resources available. Fortunately, when integrating with GenPro every interface can be simulated separately and with unique RCWA setting (i.e. number of layers and Fourier modes). For this case specifically, the simulation domain for the GIGS- Mo interface could have been simplified significantly. As the period of the metal interface texture is just 33nm.

Additionally, computer resources are often times the bottle neck with respect to the simulation complexity. In RCWA we can adapt several factors to adjust the computational complexity of the simulation: number of Fourier modes, number of layers, and local E-field resolution. The standard RCWA (without local E-field) is much more memory efficient due to the S-matrix formulation. We are then limited by the large permittivity function as this grows quadratically with the number of Fourier modes, and linearly with the number of layers. If the local E-field calculation is desired, we must save the S-matrix parameters for every layer. This significantly increases the memory resources needed. The resolution of the E-field has a linear effect on memory resources as well as computational time.

For the CIGS simulation, our large domain and high E-field resolution was the largest contributing factor to the simulation time. Contrarily, for the Ray vs RCWA simulations (section 4.1.2), the local field was not needed thus the simulation time was dominated by the number of Fourier modes used. The simulation time with high number of modes became so long that further analysis of this topic was not pursued. Nevertheless, computer resources are ever expanding, and the ability to model materials with very high resolution and Fourier modes will be possible in the future.

Lastly, a few key takeaways with respect to RCWA settings:

- The height matrix of your texture needs to be very high resolution. From this, the Fourier transform is taken and an inadequate resolution will give an inaccurate Fourier transform if very thin layers are used.
- Larger textures require more layers to overcome the staircase effect.
- Materials with high complex permittivity need a high number of Fourier modes to overcome instabilities.
- Local E-field calculations can be unstable if an insufficient number of modes are used.

4.3. Conclusion

We have proven validity of RCWA over a large wavelength range through the comparison with a FEM analysis previously conducted by Rezaei et al. [33]. Additionally, we have seen the ability of RCWA to integrate fully with GenPro4 and overcome the drawback of the current wave model (SSM) by producing an accurate scatter matrix for a binary grating. Unfortunately, we were not able to demonstrate convergence between wave and ray optics, as the system becomes too large for RCWA to simulate. For very small textures, RCWA converges with the GenPro4 flat model as is expected for sufficiently small textures. In the next chapter we will present a case study of perovskite/silicon tandem cell to further demonstrate the ability of GenPro4 plus RCWA to quickly and accurately optimize nano-textured interface.

5

Perovskite/Silicon Tandem Cell

In this chapter we will present a case study of a perovskite/silcion tandem cell. The aim of this case study is to demonstrate the ability of the new RCWA plus GenPro4 to quickly and easily model real world cell structures. This will be achieved through simulating a perovskite/silicon tandem cell as presented by Jäger et al. [35], and by comparing a variety of interfaces morphologies to improve overall cell performance. We will first introduce some modification made to the RCWA code to better integrate with GenPro4.

5.1. Integration with GenPro4

Up until now we have demonstrated the validity of only the RCWA model. However, the goal of this research is to demonstrate how RCWA can be properly integrated into GenPro4. To achieve this we must first adapt the RCWA code used in the previous validation to better integrate with GenPro4. Other then slight modification to incorporate GenPro4's input variables (i.e. refractive index, coatings, and texture height matrix), we also have to adjust the simulation of the reflection and transmission regions.

In the previous validation, the incident/refection region was air. With an extinction coefficient of zero, air is non-absorbing medium. This allows us to easily calculate the reflected field as the incident field is of unit amplitude and completely real. However, if the incident medium is absorbing, the incident field become non-unitary and this leads to errors in our reflection, transmission, and absorption calculations. To overcome this issue we will ignore the complex portion of the refractive index. This will allow us to use RCWA at interfaces embedded in the solar cell, where the incident medium is also a dielectric. It should be noted that this could lead to slightly inaccurate reflection and transmission values if the incident medium is highly absorbing.

Lastly, GenPro4 currently does not provide a method of outputting the absorption of the transmission layer as this would not be compatible with the calculation of depth resolved generation profile. Therefore, the complex refractive index for the transmission region will also be ignored. This will allow all the light to pass through to the following layer and allows GenPro4 to determine the absorption. Similarly, this will also affect the transmission and reflection values calculated by RCWA. This can be demonstrated by plotting the reflection values for a variety of extinction coefficients for a planar air/perovskite interface, given in figure 5.1.

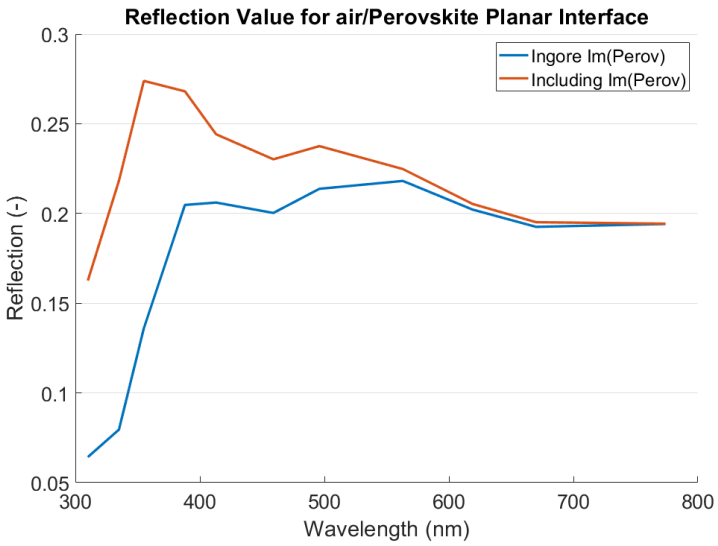

Figure 5.1: Reflection values for air/perovskite planar interface for varying wavelength. With extinction coefficient ignored (blue) and included (orange)

For dielectrics, such as perovskite and silicon, the complex portion of the refractive index is of the same order of magnitude as the real portion at shorter wavelengths (<400 nm). This leads to significant discrepancies in the reflection values, as is indicated by the orange line in figure 5.1. However, at longer wavelengths, the extinctions coefficient decreases an order of magnitude and leads to similar reflection values to that of non-absorbing (zero extinction coefficient) material. We must, therefore, be cautious with results at shorter wavelengths, where the extinction coefficient would lead to higher reflections than we will simulate.

5.1.1. GenPro4 Dashboard

To better understand the usability of RCWA within GenPro4 we will introduce a small portion of the dashboard used in this case study.

```
...
%interface 1: between layer 1 and 2 (air/Perovskite)
Int(1).model = 'wave';      %choose model ('ray' 'flat' or 'wave')
Int(1).Z = height_matrix;           Int(1).xy = [0.15,0.15]; %Period in um

Int(1).coat(1).med = 'LiF';
Int(1).coat(1).thi = 110;  %in nm for wave model else um

Int(1).coat(2).med = 'IZO';
Int(1).coat(2).thi = 090;  %in nm for wave model else um

Int(1).coat(3).med = 'SnO2';
Int(1).coat(3).thi = 010;  %in nm for wave model else um

Int(1).coat(4).med = 'C60';
Int(1).coat(4).thi = 023;  %in nm for wave model else um
...
```

Parameters such as structure height, layer and coating thickness, and even optical model used

can be identified and adjusted with a single line of code. The interface morphology, line 4, is given by a single matrix. This matrix can either be self generated, which was done in this case study, or taken from a atomic force microscope measurement. All coatings, lines 6-16, are places on-top of the interface and form conformal textured layers. Given table 5.1 and minimal coding knowledge, all data used in this case study can be easily reproduced with just two days of simulations. This helps demonstrate the usability of RCWA in future solar cell design. A full overview of the code used, with further explanation, can be found in appendix B.

5.2. Simulations

All simulations will be done with GenPro4, with the nano-sine form textured being modeled using RCWA. We start with three different cell structures: all planar layers, nano-sine texture between the silicon and perovskite, and a fully textures conformal nano-sine form layers. An overview of all three cell designs can be seen in figure 5.2. Unlike the nano-sine textured interfaces described in the paper [35], we will simulate all textures with a period of 150 nm and a variety of heights: 50, 100, 200 nm. By reducing the period of the nano-textures we can reduce the number of Fourier modes needed to accurately simulate the cell. This will allow us to simulate the nano structures more quickly as only a 17 Fourier modes are needed for a texture of this size. An overview of all layers and simulation parameters is given in table 5.1.

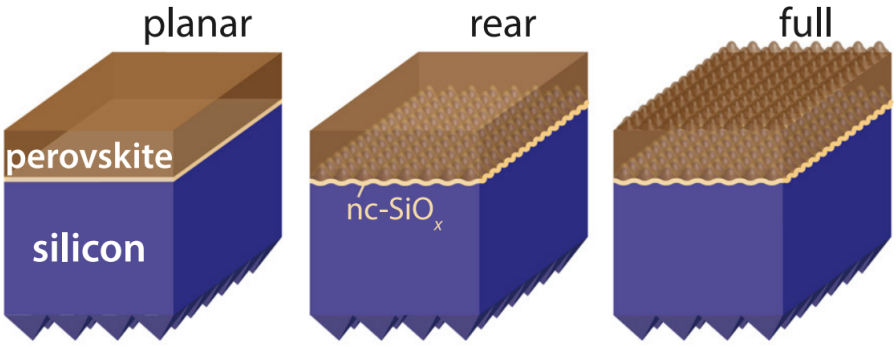

Figure 5.2: The three cell structures to be simulated using GenPro4 with RCWA [35]. The rear textured cell has nano scale sinus form between the perovskite and silicon layers. The full textured cell has has a conformal texture from the silicon layer to the top, and the planar design has only flat interfaces.

Table 5.1: All layer thickness given in manometers expect form crystalline silicon which is in micrometers [35]. Below is the RCWA settings where the number of Fourier modes is decreased at higher wavelengths to conserve time.

Lithium fluoride (LiF)	110
Indium zin oxide (IZO)	90
Tin oxide (SnO2)	10
C60	23
Perovskite	569
Indium tin oxide (ITO)	21
Nanocrystalline silicon oxide (nc-SiO)	107
Intrinsic amorphous hydrogenated Si (a-SI:H)	5
Crystalline Silicon (um)	300
Fourier modes 300-500 nm	17
Fourier modes 600-1200 nm	15
Layers	100
Local E field res. x (nm)	4
Loacl E field res. y (nm)	4
Loacl E field res. z (nm)	3

Within GenPro4, we can choose the dimension of every texture at every interface between layers. On top of these layers, coatings can be added to be simulated coherently; with RCWA if nano-textured or TMM if planar. The layers, in our case crystalline silicon and perovskite, will be simulated incoherently. It is worth noting that the coherence length of sunlight is approximately, 0.6 micrometers Lee et al. [36]. Thus the assumption that the perovskite layer can be simulated incoherently may cause inaccuracies in our results compared to experimental data. Nevertheless, it was chosen to split the cell in this way to allow for the simulation of different texture sizes between each layer: air-perovskite and perovskite-silicon.

In figure 5.3, we can see the area plot of the fully planar reference cell. Followed by figures 5.4a and 5.4b, where the different textured cell area plots are given with the mythologies as seen in figure 5.2. With a reflection value of 1.4 mA/cm^2, the fully textured cell has far superior reflection performance compared to the remaining two designs, with refection value of 2.3 mA/cm^2. However, the rear textured cell has the best performance. Tandem cells have absorption layers in series, meaning the total current of the cell is controlled by the layer with the lowest current, in our case the c-Si layer. Due to the rear textured cell having a higher current in the c-Si layer, see figure 5.4a, this cell will perform best.

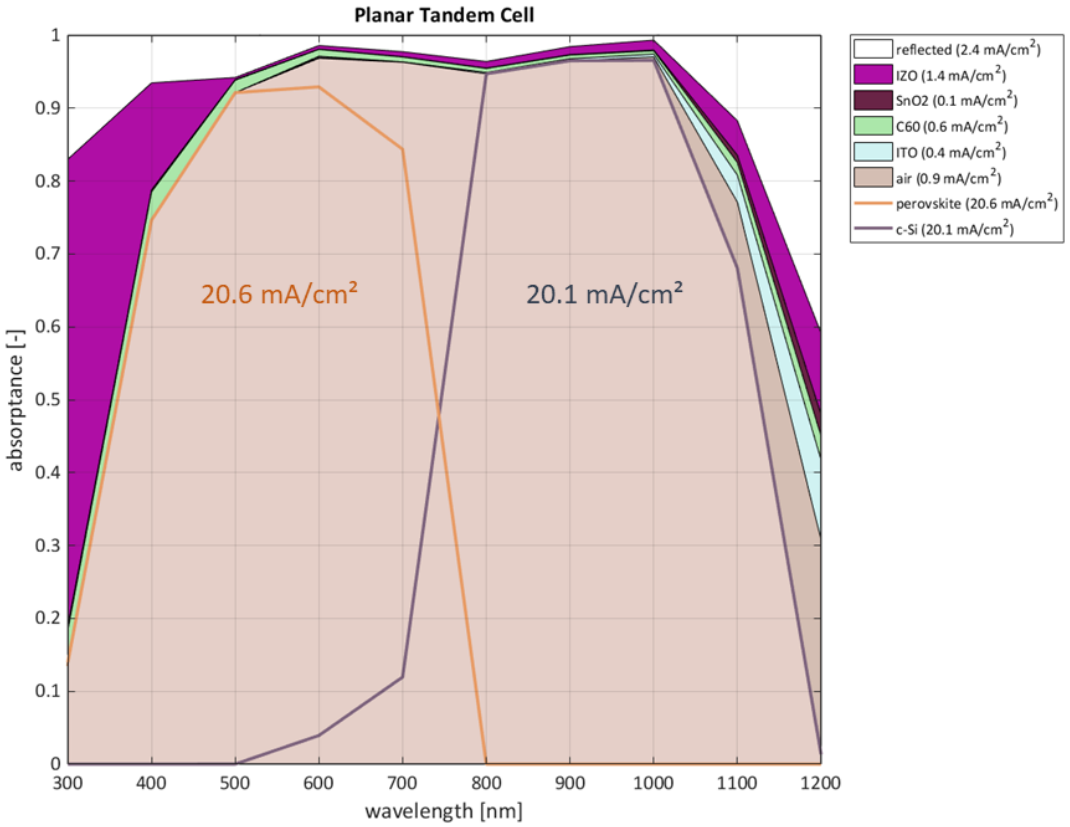

Figure 5.3: Area plots of GenPro4 with RCWA simulation of planar Perovskite/Silicon tandem cell. With the orange and purple lines representing the area absorbed by perovskite and silicon respectively.

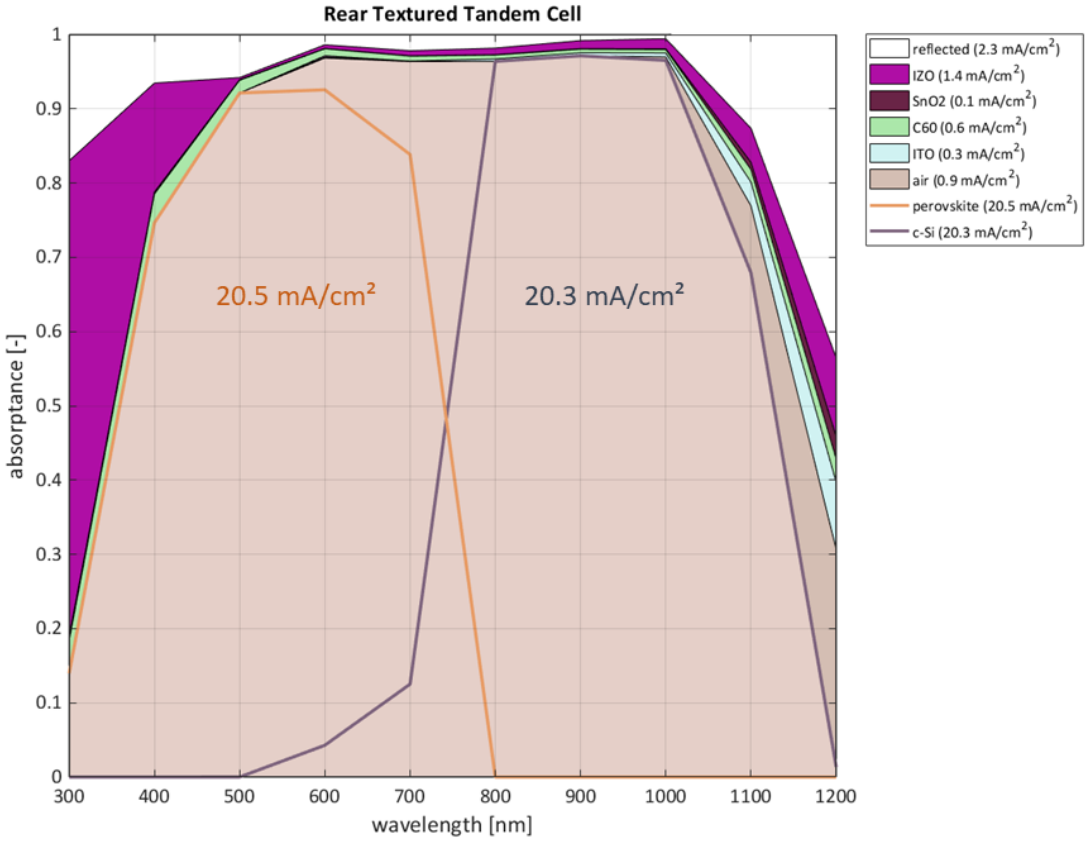

(a) With a period of 150 nm and height of 200 nm, the rear textured tandem cell area plot.

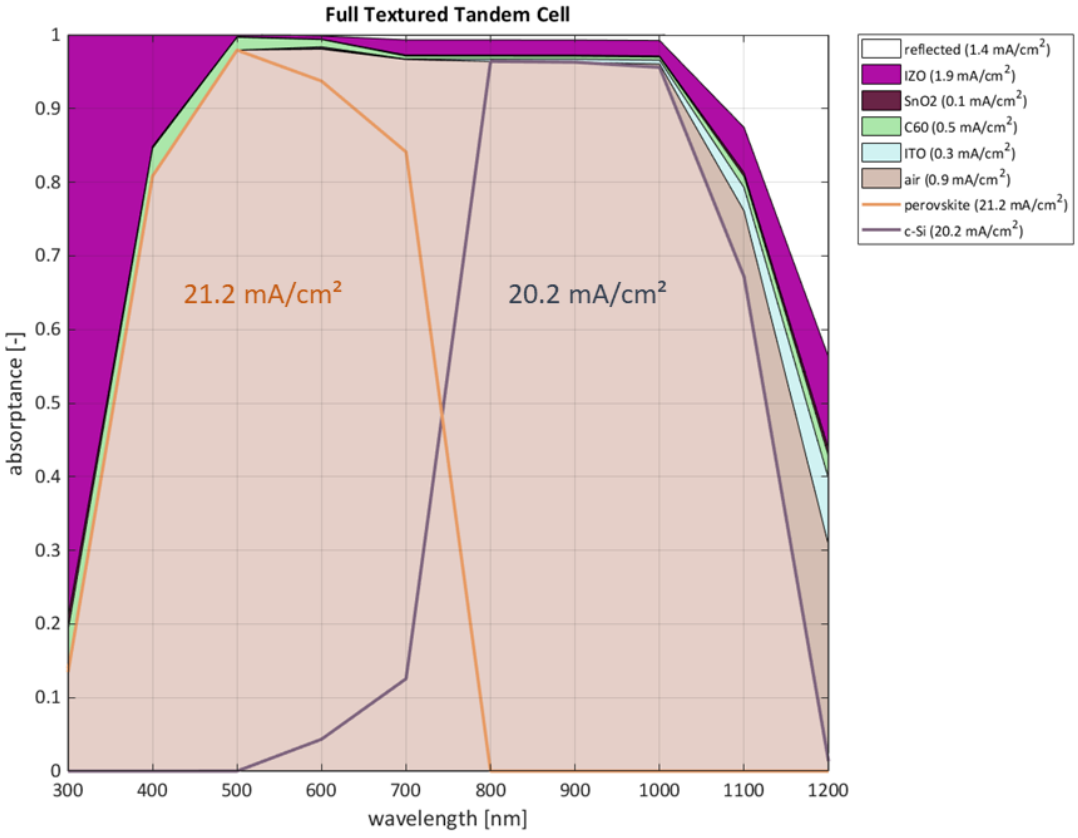

(b) The fully textured conformal tandem cell are plot, with a period of 150 nm and height of 200 nm

We will vary the texture in a single layer while keeping the other constant, this will allow us to compare all combinations of texture dimensions as given in figures 5.6. Additionally, we can see the effect on absorption by varying the fully textured design height in figure 5.5.

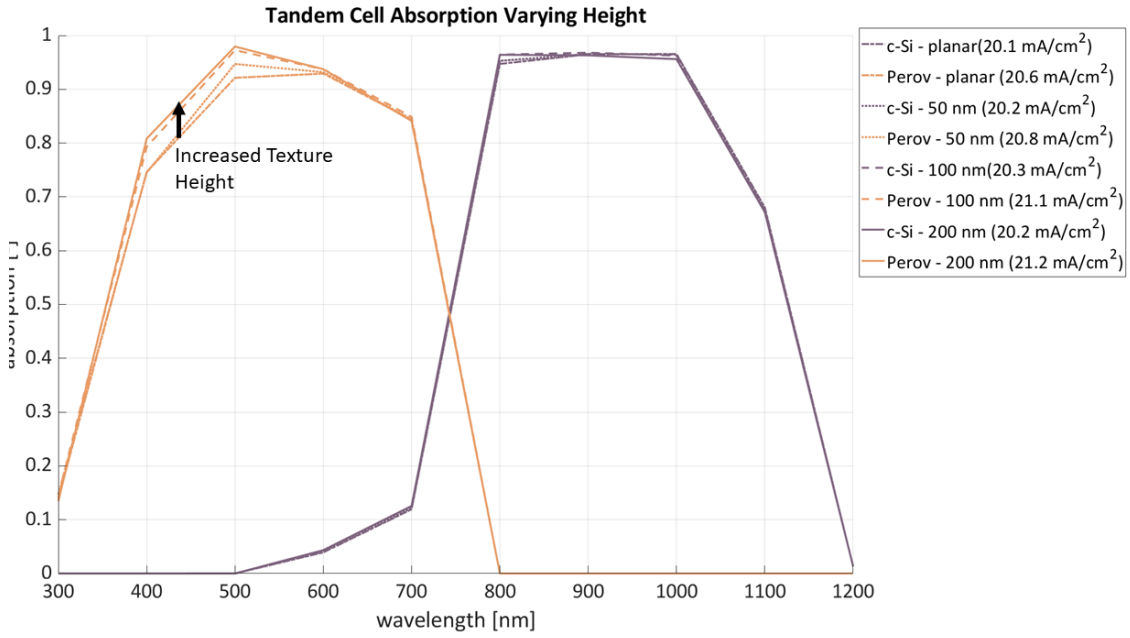

Figure 5.5: Absorption plot for a variety of texture heights. All heights are conformal for the first two interfaces: perovskite-air and perovskite-silicon. In the legend the current for every absorption layer with respect to the texture height can be seen.

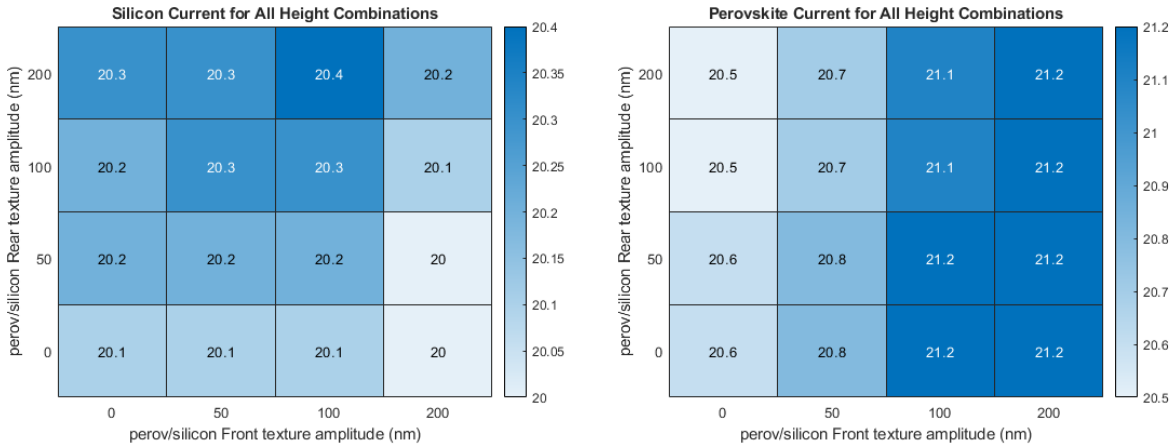

Figure 5.6: All combinations of texture heights and the respective current per absorption layer. All values are given in mA/cm^2.

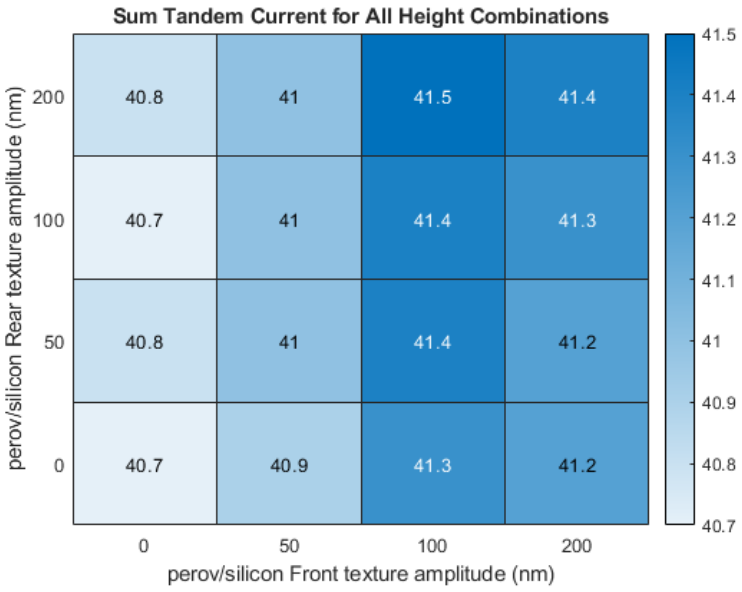

Figure 5.7: The summation of current generated in perovskite and silicon layer with varying front interface heights (x-axis) and varying rear interface heights (y-axis).

As can be seen in figure 5.6, the cell with front texture height of 100 nm and rear texture height of 200 nm has the best performance with a current of 20.4 mA/cm^2. Further performance can be gained by adjusting the layer thickness to better balance the current over both layers, this is known as current matching. To determine the performance of the current matched cell, we take the sum of the current generated in each layer as given in figure 5.7. After current matching, the total cell current will be approximately equal to the values given in figure 5.7 divided by two. Giving us an optimal performance of 20.75 mA/cm^2. A significant improvement over the 20.35 mA/cm^2 generated by the current matched planar cell. Additionally, electrical performance can also play a major role with cell design. However, nano-sine form structures on perovskite have shown to have good electrical performance [37].

5.3. Conclusion

In conclusion, we set out to demonstrate the ability of GenPro4 plus RCWA to quickly model difference nano-textured cell structures. This was achieved within just two days of simulation, allowing us to compare 16 different cell designs and choose a optimal texture size per interface. If, additionally, current matching was applied, a current increase of 2% could be realized. All simulations were achieved by only adjusting a single value for the height of the nano-texture. This truly demonstrates the ability for RCWA to be used in combination with GenPro4 without any advanced coding knowledge. Although no simulation model is perfect, RCWA is user friendly, accurate, and quick for nano-textured interfaces.

6

Conclusion and Recommendations

6.1. Conlusion

To further improve the light management and optical performance of solar cells, research into nano-textured surfaces has led to a need for fast and accurate wave optics model. Currently, within the PVMD group at the TU Delft, an optical solar cell simulation tool, GenPro4, is being developed to allow for the quick optimization and analysis of solar cell designs. However, the implemented wave optics model has limited accuracy and thus an alternative model was sought. This thesis focused on the implementation of an improved wave optics model, and the following research question were answered:

- *What alternative wave optics model is best suited for integration with GenPro4?*
  Several alternative models were investigated and compared. The models were chosen based on three selection criteria: speed, accuracy, and compatibility. Due to its robust nature and adaptive complexity, the rigorous couple wave analysis (RCWA) was chosen. This model has increased in popularity as stability improvements and numerical efficiencies have been recently published. RCWA allows the user to choose the computational complexity by adapting the number of Fourier modes and sublayers used. Allowing us to accurately simulate small nano-textures within several seconds, thus, much faster than alternative modes (FEM or FDTD). Additionally, this model can be fully integrated into MATLAB together with GenPro4. A single program can be used to model all forms of interface texturing adding to the compatibility of this method.

- *Can any speed or accuracy improvements be made?*
  By implementing the S-matrix formulation of RCWA we have increased the memory efficiency and speed. To fully integrate with GenPro4, we modified the output to generate reflection and transmission angle intensity distributions known as scatter matrices. Additionally, the local E-field was calculated to determine the absorption per unit volume in our simulation domain, thus increasing the accuracy. This allows GenPro4 to determine the current generated per material in our device. All these improvements over the standard RCWA allow for a fast and accurate integration with GenPro4.

- *What computational or accuracy limits, if any, does the new model face?*
  To validate our version of RCWA we simulated a CIGS cell with nano-textured interfaces. The results were compared to a previously conducted FEM analysis. We saw good agree-

ment between the two models over a large wavelength range. However, the molybdenum back reflector proved difficult to simulate leading to an absorption error of 12% for this layer. To overcome this discrepancy, potentially several hundred Fourier modes were needed for an accurate simulation. As this was not possible with the given computational resources, a clear limitation was discovered: highly absorbing materials, such as metals, can not accurately be simulated given the current computer resources. Furthermore, we successfully simulated the angle distribution from a binary grating to prove the ability of RCWA to overcome a limitation of the previous wave model. An additional limitation was discovered when trying to simulate large micro-textures as these also require far more Fourier modes, and thus computer memory, than the computer resources allowed.

Lastly, we presented a case study to demonstrated the fully incorporated RCWA plus GenPro4 model by simulating a perovskite/silicon tandem cell with nano-sine interfaces. Within two days, 16 combinations of structure height were simulated and compared, and an optimal height per interface was discovered. This exemplifies the ability of our new wave model to accurately and easily be used in real world cell design. We have, therefore, achieved our research goal of implement an improved wave optics model into GenPro4.

6.2. Recommendations

Lastly, a few recommendations are given below:

- Currently, only absorption in coating is able to be given to GenPro4. We can improve the accuracy of the wave optics simulation by incorporating absorption for transmission region. The RCWA method is already able to do this, but GenPro4 does not yet support this information. It is recommended to implement this as it would provide a more accurate result.
- Further research into the transition from wave to ray optics for nano- to micro-textures to better understand at which scale RCWA is valid. To start, the simulation done by Lokar et al. [19] can be recreated.
- Implement adaptive Fourier modes. As we transition through the wavelength range we can adjust the number of Fourier modes to speed up the total simulation.
- Due to the difficulty of knowing the number of Fourier modes necessary to accurately simulate a specific structure/material it is recommend to create a database where previous simulation parameters can be recorded and used as indicator for future simulation parameters.
- Lastly, re-run the validation simulation with the fully integrated RCWA plus GenPro4 to determine if a metal interface with sufficiently small period can be modeled with current computer resources.

Bibliography

[1] L. C. Andreani, A. Bozzola, P. Kowalczewski, M. Liscidini, and L. Redorici. Silicon solar cells: toward the efficiency limits. *Advances in Physics: X*, 4(1):1548305, 2019.

[2] A. Vossier, F. Gualdi, A. Dollet, R. Ares, and V. Aimez. Approaching the shockley-queisser limit: General assessment of the main limiting mechanisms in photovoltaic cells. *Journal of Applied Physics*, 117(1):015102, 2015.

[3] J.-Q. Xi, M. F. Schubert, J. K. Kim, E. F. Schubert, M. Chen, S.-Y. Lin, W. Liu, and J. A. Smart. Optical thin-film materials with low refractive index for broadband elimination of fresnel reflection. *Nature photonics*, 1(3):176–179, 2007.

[4] R. Santbergen, T. Meguro, T. Suezaki, G. Koizumi, K. Yamamoto, and M. Zeman. Genpro4 optical model for solar cell simulation and its application to multijunction solar cells. *IEEE journal of photovoltaics*, 7(3):919–926, 2017.

[5] W.-K. Kuo, J.-J. Hsu, C.-K. Nien, and H. H. Yu. Moth-eye-inspired biophotonic surfaces with antireflective and hydrophobic characteristics. *ACS applied materials & interfaces*, 8 (46):32021–32030, 2016.

[6] K. Jäger. *On the scalar scattering theory for thin-film solar cells*. PhD thesis, Delft University of Technology, 2012. URL https://doi.org/10.4233/uuid:4220e3ee-bdcb-4a46-ade1-470d3c2ad6da.

[7] K. Han and C.-H. Chang. Numerical modeling of sub-wavelength anti-reflective structures for solar module applications. *Nanomaterials*, 4(1):87–128, 2014.

[8] M. Paulsen, L. T. Neustock, S. Jahns, J. Adam, and M. Gerken. Simulation methods for multiperiodic and aperiodic nanostructured dielectric waveguides. *Optical and quantum electronics*, 49(3):107, 2017.

[9] S. Chattopadhyay, Y.-F. Huang, Y.-J. Jen, A. Ganguly, K. Chen, and L. Chen. Anti-reflecting and photonic nanostructures. *Materials Science and Engineering: R: Reports*, 69(1-3):1–35, 2010.

[10] M. Plakhotnyuk. Nanostructured heterojunction crystalline silicon solar cells with transition metal oxide carrier selective contacts. 2018.

[11] B. W. Schneider, N. N. Lal, S. Baker-Finch, and T. P. White. Pyramidal surface textures for light trapping and antireflection in perovskite-on-silicon tandem solar cells. *Optics express*, 22(106):A1422–A1430, 2014.

[12] S. Berthier and J. Lafait. Effective medium theory: mathematical determination of the physical solution for the dielectric constant. *Optics Communications*, 33(3):303–306, 1980.

[13] Y. E. B. Vidhya and N. J. Vasa. Numerical and experimental analysis of nano second laser

induced surface textures for light trapping in a-si thin film for solar cells. *Materials Research Express*, 5(6):066410, 2018.

[14] R. Santbergen, J. Goud, M. Zeman, J. van Roosmalen, and R. C. van Zolingen. The am1. 5 absorption factor of thin-film solar cells. *Solar energy materials and solar cells*, 94(5): 715–723, 2010.

[15] R. Siegel. Net radiation method for transmission through partially transparent plates. 1973.

[16] R. J. Potton. Reciprocity in optics. *Reports on Progress in Physics*, 67(5):717–754, apr 2004. doi: 10.1088/0034-4885/67/5/r03. URL https://doi.org/10.1088/0034-4885/67/5/r03.

[17] M. Zeman, R. Van Swaaij, J. Metselaar, and R. Schropp. Optical modeling of a-si: H solar cells with rough interfaces: Effect of back contact and interface roughness. *Journal of Applied Physics*, 88(11):6436–6443, 2000.

[18] R. De Rose, M. Zanuccoli, P. Magnone, E. Sangiorgi, and C. Fiegna. Open issues for the numerical simulation of silicon solar cells. In *Ulis 2011 Ultimate Integration on Silicon*, pages 1–4, 2011. doi: 10.1109/ULIS.2011.5757961.

[19] Z. Lokar, B. Lipovsek, J. Krc, et al. Performance analysis of rigorous coupled-wave analysis and its integration in a coupled modeling approach for optical simulation of complete heterojunction silicon solar cells. *Beilstein journal of nanotechnology*, 9(1):2315–2329, 2018.

[20] S. C. Kim. Simulation of rough surface of cigs (cuingase) solar cell by rcwa (rigorous coupled wave analysis) considering the incoherency of light. *J. Opt. Soc. Korea*, 18(2): 180–183, Apr 2014. URL http://www.osapublishing.org/josk/abstract.cfm?URI=josk-18-2-180.

[21] D. Lehr, M. Helgert, M. Sundermann, C. Morhard, C. Pacholski, J. P. Spatz, and R. Brunner. Simulating different manufactured antireflective sub-wavelength structures considering the influence of local topographic variations. *Opt. Express*, 18(23):23878–23890, Nov 2010. doi: 10.1364/OE.18.023878. URL http://www.opticsexpress.org/abstract.cfm?URI=oe-18-23-23878.

[22] M. Agrawal and M. Frei. Rigorous optical modeling and optimization of thin-film photovoltaic cells with textured transparent conductive oxides. *Progress in Photovoltaics: Research and Applications*, 20(4):442–451, 2012.

[23] C.-C. Chung, H.-C. Lo, Y.-K. Lin, H.-W. Yu, B. T. Tran, K.-L. Lin, Y. C. Chen, N.-H. Quan, E. Y. Chang, and Y.-C. Tseng. Broadband antireflection sub-wavelength structure of ingap/ingaas/ge triple junction solar cell with composition-graded sinx. *Materials Research Express*, 2(5):055505, 2015.

[24] A. F. Oskooi, D. Roundy, M. Ibanescu, P. Bermel, J. D. Joannopoulos, and S. G. Johnson. MEEP: A flexible free-software package for electromagnetic simulations by the FDTD method. *Computer Physics Communications*, 181:687–702, January 2010. doi: 10.1016/j.cpc.2009.11.008.

[25] S. Feilmeier, wgerbl, ebakir, fabianfnc, huseyinsaht, pooran c, M. Obermeier, sebastianasen, Sagar, Kyle, luzpaz, L. Kaindl, ahummelsberger, lukas-bender rodriguez, C. Lehne, AlexanderHollandFenecon, L. Verhovskij, M. Grüning, greemo, D. Jasselette, A. Fischer, Anita4Schmid, A. Braovic, JohannesHundschell, WolfgangMiethaner, angular cli, denis-jidovtseff jc, and fgarlin. Openems/openems: 2021.4.0, February 2021. URL https://doi.org/10.5281/zenodo.4564858.

[26] M. Moharam, E. B. Grann, D. A. Pommet, and T. Gaylord. Formulation for stable and efficient implementation of the rigorous coupled-wave analysis of binary gratings. *JOSA a*, 12(5):1068–1076, 1995.

[27] M. Auer. *Numerical treatment of localized fields in rigorous diffraction theory and its application to light absorption in structured layers*. Dissertation, Heidelberg University, 2016. URL https://doi.org/10.11588/heidok.00021440.

[28] R. C. Rumpf. Improved formulation of scattering matrices for semi-analytical methods that is consistent with convention. *Progress In Electromagnetics Research*, 35:241–261, 2011.

[29] G. Kajtar. *Electromagnetic properties of double-periodic structures*. PhD thesis, SLOVAK UNIVERSITY OF TECHNOLOGY IN BRATISLAVA, 2014. URL https://rawdogapp.weebly.com/uploads/2/3/1/9/23191398/dissertation_thesis.pdf.

[30] K.-H. Brenner. Aspects for calculating local absorption with the rigorous coupled-wave method. *Optics express*, 18(10):10369–10376, 2010.

[31] H. Kim, I.-M. Lee, and B. Lee. Extended scattering-matrix method for efficient full parallel implementation of rigorous coupled-wave analysis. *JOSA A*, 24(8):2313–2327, 2007.

[32] L. Li. Formulation and comparison of two recursive matrix algorithms for modeling layered diffraction gratings. *JOSA A*, 13(5):1024–1035, 1996.

[33] N. Rezaei, O. Isabella, P. Procel, Z. Vroon, and M. Zeman. Optical study of back-contacted cigs solar cells. *Optics express*, 27(8):A269–A279, 2019.

[34] V. Fitio, I. Yaremchuk, A. Bendzyak, and Y. Bobitski. Modified rcwa method for studying the resonance diffraction phenomena on metal gratings. In *2017 IEEE 37th International Conference on Electronics and Nanotechnology (ELNANO)*, pages 170–174, 2017. doi: 10.1109/ELNANO.2017.7939741.

[35] K. Jäger, J. Sutter, M. Hammerschmidt, P.-I. Schneider, and C. Becker. Prospects of light management in perovskite/silicon tandem solar cells. *Nanophotonics*, 10(8):1991–2000, 2020.

[36] G. Lee, J. Kim, S. Kim, and J. Kim. Effect of the incoherent encapsulation layer and oblique sunlight incidence on the optical and current-voltage characteristics of surface-textured cu (in, ga) se2 solar cells based on the angle-dependent equispaced thickness averaging method. *Applied Sciences*, 11(5):2121, 2021.

[37] P. Tockhorn, J. Sutter, R. Colom, L. Kegelmann, A. Al-Ashouri, M. Roß, K. Jager, T. Unold, S. Burger, S. Albrecht, et al. Improved quantum efficiency by advanced light management in nanotextured solution-processed perovskite solar cells. *ACS Photonics*, 7(9):2589–2600, 2020.

A

RCWA Derivations

In this chapter some derivations of RCWA components will be explained. These will give the user further in site into the specific formulation used in this form of RCWA.

A.1. S-matrix

By choosing the $\hat{z}$ to be equal to zero at every interface, the exponential term in equation 3.18 equals to zero expect within layer i. We can now use the generalized field equation (3.18) to solve for the scatter matrix values within layer i.

$$\begin{bmatrix} \mathbf{W_1} & \mathbf{W_1} \\ -\mathbf{V_1} & \mathbf{V_1} \end{bmatrix} \begin{bmatrix} C_1^f \\ C_1^b \end{bmatrix} = \begin{bmatrix} \mathbf{W_i} & \mathbf{W_i} \\ -\mathbf{V_i} & \mathbf{V_i} \end{bmatrix} \begin{bmatrix} C_i^f \\ C_i^b \end{bmatrix} \tag{A.1}$$

$$\begin{bmatrix} \mathbf{W_i} & \mathbf{W_i} \\ -\mathbf{V_i} & \mathbf{V_i} \end{bmatrix} \begin{bmatrix} e^{-\boldsymbol{\lambda}\hat{z}} & 0 \\ 0 & e^{\boldsymbol{\lambda}\hat{z}} \end{bmatrix} \begin{bmatrix} C_i^f \\ C_i^b \end{bmatrix} = \begin{bmatrix} \mathbf{W_2} & \mathbf{W_2} \\ -\mathbf{V_2} & \mathbf{V_2} \end{bmatrix} \begin{bmatrix} C_2^f \\ C_2^b \end{bmatrix} \tag{A.2}$$

By substituting equation A.1 into equation A.2 and rearranging the terms to match the scatter matrix form (eq3.23), we are left with

$$\begin{aligned} S_{11}^i &= (A_{i1} - X_i B_{i2} A_{i2}^{-1} X_i B_{i1})^{-1} (X_i B_{i2} A_{i2}^{-1} X_i A_{i1} - B_{i1}) \\ S_{12}^i &= (A_{i1} - X_i B_{i2} A_{i2}^{-1} X_i B_{i1})^{-1} X_i (A_{i2} - B_{i2} A_{i2}^{-1} B_{i2}) \\ S_{21}^i &= (A_{i2} - X_i B_{i1} A_{i1}^{-1} X_i B_{i1})^{-1} X_i (A_{i1} - B_{i1} A_{i1}^{-1} B_{i1}) \\ S_{22}^i &= (A_{i2} - X_i B_{i1} A_{i1}^{-1} X_i B_{i1})^{-1} (X_i B_{i1} A_{i1}^{-1} X_i A_{i2} - B_{i2}) \end{aligned} \tag{A.3}$$

$$\begin{aligned} A_{ij} &= \mathbf{W}_i^{-1} \mathbf{W}_j + \mathbf{V}_i^{-1} \mathbf{V}_j \\ B_{ij} &= \mathbf{W}_i^{-1} \mathbf{W}_j - \mathbf{V}_i^{-1} \mathbf{V}_j \end{aligned} \tag{A.4}$$

$$X_i = e^{-\boldsymbol{\lambda} k_0 L_i} \tag{A.5}$$

We can now simplify this formualtion by surrounding each layer with a zero thickness vacuum layer. Since a vacuum is homogeneous and has unitary permitivity, the S-matrices become:

$$\begin{aligned} S^i_{11} = S^i_{22} &= (A_{i1} - X_i B_{i2} A^{-1}_{i2} X_i B_{i1})^{-1} (X_i B_{i2} A^{-1}_{i2} X_i A_{i1} - B_{i1}) \\ S^i_{12} = S^i_{21} &= (A_{i1} - X_i B_{i2} A^{-1}_{i2} X_i B_{i1})^{-1} X_i (A_{i2} - B_{i2} A^{-1}_{i2} B_{i2}) \end{aligned} \tag{A.6}$$

$$\begin{aligned} A_{ij} &= \mathbf{W}_i^{-1}\mathbf{W}_0 + \mathbf{V}_i^{-1}\mathbf{V}_0 \\ B_{ij} &= \mathbf{W}_i^{-1}\mathbf{W}_0 - \mathbf{V}_i^{-1}\mathbf{V}_0 \end{aligned} \tag{A.7}$$

Each layer S-matrix can now be computed with a single eigenvalue problem for the current layer i as well as the eigenvalues of free space given by $\mathbf{W}_0$ and $\mathbf{V}_0$.

A.2. Wave K vector

The wave vector k represents the Fourier decomposition of a plane wave. All allowed wave modes can be determined using the grating equation as given bellow:

$$\begin{aligned} k_x(p) &= k_{x,inc} - \frac{k_0 p \lambda}{P_x} \\ k_{inc} &= k_0 n_1 (sin(\theta)cos(\phi), sin(\theta)sin(\phi), cos(\theta)) \end{aligned} \tag{A.8}$$

With k_0 the free space wave number as previously defined, λ the wavelength, and P_x the period structure in the x direction. The wave modes m are integer values between $-\infty$ and ∞. These mode coefficients create a diffraction pattern around the spectral (zero order) mode given by $k_{x,inc}$. A similar equation can be derived for the y direction by replacing all x values with y and m with n. The incident wave vector in Cartesian coordinates is given by k_{inc}, where θ and ϕ equaling the polar and azimuth angles of the incident light.

The z component can be determined via the following equation

$$\begin{aligned} k^2_{z,ref,trn} &= k^2_x + k^2_y + k^2_z \\ k_{z,ref,trn} &= \frac{2\pi}{\lambda} n_{ref,trn} \\ k_{z,ref,trn}(p,q) &= \sqrt{k_0^2 n_{ref,trn} - k_x^2(p) - k_y^2(q)} \end{aligned} \tag{A.9}$$

The longitudinal wave vector (k_z) needs to be calculated for both the reflection and transmission regions. If the reflection medium is losses, n_{ref} is purely real, $k_{z,ref}$ will be either fully real or fully imaginary. When the values become imaginary the wave corresponds to an evanescent wave, or in other words, non-propagating waves. If a absorbing material is being simulated, k_z will always be complex due to the refractive index being a complex number. However, when the real part become zero this again corresponds to an evanescent wave.

Clearly, a infinite number of wave modes is not possible to simulate, thus truncation needs to take place. As can be seen in equation A.9, the x and y wave vectors are now limited to p and q respectively. With p now being integers between $-M$ and M. This leads to a total number of modes in x direction $p = 2M+1$. Similarly, the toal number of modes in the y direction is now $q = 2N+1$. The longitudinal wave vector k_z needs to be calculated for every combination of k_x and k_y. This can easily be done by using the MATLAB function $meshgrid(k_x, k_y)$. This leads to the 2D arrays given below

$$k_x = \left[\underbrace{k_{x,-M}, k_{x,-M+1}, \ldots, k_{x,M-1}, k_{x,M}}_{\text{Repeat q Times}}, \ldots \right]^T \tag{A.10}$$

$$k_y = \left[\underbrace{k_{y,-N}, k_{y,-N}, \ldots, k_{y,-N}, k_{y,-N}}_{\text{Repeat p Times}}, \ldots, k_{y,N}, k_{y,N} \right]^T \tag{A.11}$$

The k_x array consists of all the wave modes in order and then repeated q time to give a total number of elements equal to pq. The k_y array is generated by repeating a all wave mode q times in increasing order, thus also leading to an array size of pq. These two arrays can now be placed into a diagonal matrices of total size $pq \times pq$. This is an important steps as all calculations need to be done for all allowed wave modes. By placing the x and y components into diagonal matrices, all calculations can be easily done with matrix algebra. The matrix form of $k_x$and k_y are donated by $\mathbf{K}_x$ and $\mathbf{K}_y$ respectively.

A.3. Local E Field

Here a we will walk through the method of determining the loval E field value at every point in our simulation domain. To start we need z components of the eigenvectors $\mathbf{W}_z$ and $\mathbf{V}_z$

$$\mathbf{W}_z = [\epsilon]^{-1}[-K_y, K_x]\mathbf{V} \tag{A.12}$$

$$\mathbf{V}_z = [-K_y, K_x]\mathbf{W} \tag{A.13}$$

We now know how the wave propagate (their eigenvectors) and with how much energy (their eigenmodes). The last thing we need to determine is the phase shift at every point in our device

$$\phi_x(x) = e^{-k_0 K_x x} \tag{A.14}$$

A similar equation can be determined for the y direction. In the z direction the phase shift is determined by the calculated eigenvalues λ_i, thus varying per layer.

$$\phi_z(z) = e^{-k_0 \lambda_i z} \tag{A.15}$$

$$\Phi_z(z) = \begin{pmatrix} \phi_z(z) & 0 \\ 0 & \phi_z(L)\phi_z(-z) \end{pmatrix} \tag{A.16}$$

The z phase component needs to be given in this way because it represents the forward and backward propagating waves, as also is given by the forward and backward propagation wave modes $\mathbf{C}_i$ We can now form the final formula in a similar from to equation 3.18.

$$\Phi_{xyz} = \phi_x \phi_y \mathbf{M} \Phi_z \mathbf{C}_i \tag{A.17}$$

Matrix $\mathbf{M}$ represents the eigenvectors of all wave components:

$$\mathbf{M} = \begin{bmatrix} \mathbf{W} & \mathbf{W} \\ -\mathbf{W}_z & \mathbf{W}_z \\ -\mathbf{V} & \mathbf{V} \\ \mathbf{V}_z & \mathbf{V}_z \end{bmatrix} \tag{A.18}$$

B

Case Study Example and Code

Here we will present the GenPro4 dashboard as used in the case study. Due to size of the RCWA code, this will not be presented in this thesis. However, all components have been presented in chapter 3 and appendix A.

```
clear Lay Int                                %clear workspace

load('AFM.mat','pyramids_20um')  %load 20x20um height map

%===LAYERS===
Lay(1).med = 'air';                          Lay(1).thi = inf;
Lay(2).med = 'perovskite';                   Lay(2).thi = 0.569;
Lay(3).med = 'c-Si';                         Lay(3).thi = 300;
Lay(4).med = 'air';                          Lay(4).thi = inf;

%===INTERFACES===
Lx= 1000; %resolution of height matrix
h0 = 50; %sine height
height_matrix = Nano_sine(Lx,h0);
%interface 1: between layer 1 and 2 (air/Perov)
Int(1).model = 'wave';              %choose model ('ray' 'wave 'flat')
Int(1).Z = height_matrix;    Int(1).xy = [0.15,0.15]; %period in um

Int(1).coat(1).med = 'LiF';
Int(1).coat(1).thi = 110;  %*in nm for wave model

Int(1).coat(2).med = 'IZO';
Int(1).coat(2).thi = 090;  %*in nm for wave model

Int(1).coat(3).med = 'SnO2';
Int(1).coat(3).thi = 010;  %*in nm for wave model

Int(1).coat(4).med = 'C60';
Int(1).coat(4).thi = 023;  %*in nm for wave model

%interface 1: between layer 1 and 2 (Perov/c-Si)
Int(2).model = 'wave';
Int(2).Z = height_matrix;    Int(2).xy = [0.15,0.15]; %period in um
Int(2).coat(1).med = 'ITO';
```

```
35 Int(2).coat(1).thi = 021;  %*in nm for wave model
36
37 Int(2).coat(2).med = 'a-SiOx';
38 Int(2).coat(2).thi = 107;  %*in nm for wave model
39
40 Int(2).coat(3).med = 'a-Si_i';
41 Int(2).coat(3).thi = 005; %*in nm for wave model
42
43 %interface 2: between layer 2 and 3 (c-Si/air)
44 Int(3).model = 'ray';            %use RAY-optics model
45 Int(3).Z = -pyramids_20um;       Int(3).xy = [20,20];   %period in um
46 %=====================
47 S.wav = 00.3000:0.1:1.20;
48 S.n_rays = 100;
49
50 [Lay,Int,out] = GENPRO4(Lay,Int,S);           %run simulation
51
52 function height_matrix = Nano_sine(Lx,h0)
53
54 height_matrix= zeros(Lx,Lx);
55 for i = 1:Lx
56     for j=1:Lx
57         height_matrix(i,j) =  h0/2*(1+cos(2*pi*i/Lx)*cos(2*pi*j/Lx));
58     end
59 end
60 end
```

To start, we must introduce all layers in our device. Layers are calculated using GenPro4 and are always modeled incoherently. The first and last layer are always of infinite thickness, the remaining layers thickness is given in micrometers.

Next, we must determine the interface textures. In this case we generate our own height matrix via the function Nano_sine (lines 52-60). It is very important to use a sufficiently high resolution grid, as this is crucial for an accurate Fourier transform. If this is not done, instabilities can occur if a high number of layers is used.

Alternatively, we can use a atomic force microscope (AFM) measurement for our height matrix. This is done in line 44 for the micro-textured silicon/air interface. Again, if AFM data is used for the wave model, care needs to be taken to ensure high resolution. Thus, interpolation of data may be needed.

For the wave model, all coating thickness need to be given in manometers, this includes the height matrix. Contrarily, the period can be given in micrometers. An arbitrary number of coatings can be added to an interface. All coatings are conformal to the height matrix and are numbered from top to bottom. For example, LiF is the top coating and C60 is directly on top of the perovskite layer. A figure of the real values in the permittivity matrix is given below:

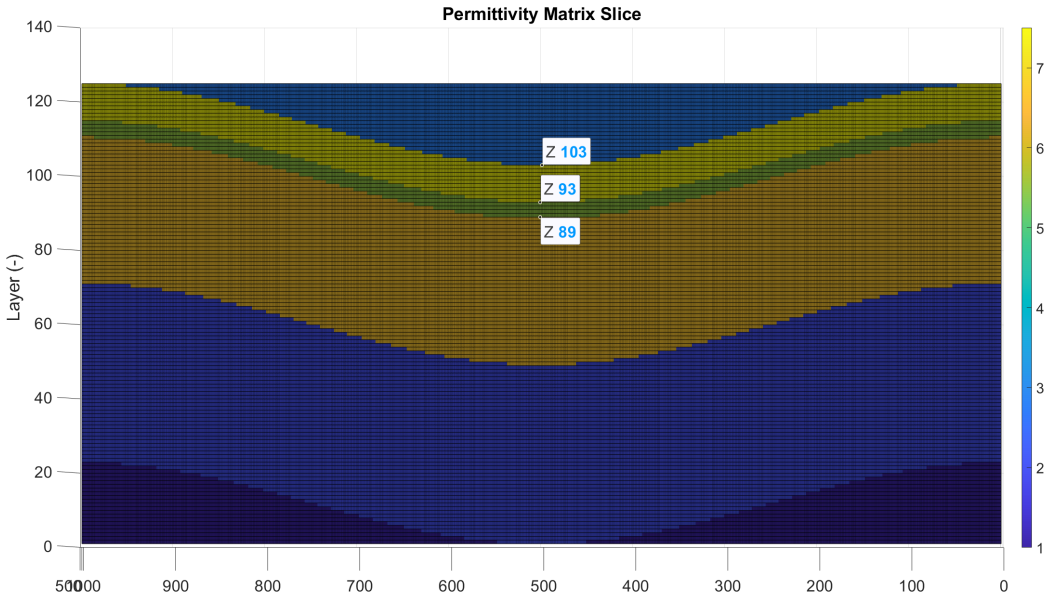

Figure B.1: Slice of the real values of permittivity matrix for sine texture with height of 50 nm.

The permittivity matrix is inverted to ensure that layer 1 of our permittivity matrix corresponds to the top of our interface plus coatings. We can also check the thickness of each layer by following these simple steps:

$$\text{Number of layers} = 125 \tag{B.1}$$

$$\text{total interface thickness (nm)} = 50 + 110 + 90 + 10 + 23 = 283 \tag{B.2}$$

$$\text{thickness per layer} = 283/125 = 2.264\text{nm} \tag{B.3}$$

$$\text{thickness of last coating (C60)} = (103 - 93) * 2.264 = 10 * 2.264 = 22.64\text{nm} \tag{B.4}$$

We calculated a thickness of 22.64 nm. The discrepancy with the actual value of 23 nm is due to the limited number of layers. Additionally, a clear staircase effect can be seen in figure B.1. Both issues can be reduced with additional layers. However, visual inspection (such as this) will not help determine the accuracy of simulations.

Lastly, simulation of a new morphology can easily be done by modifying either the height (line 13) or period of the sine texture (lines 17 and 33). Additionally, new GenPro4 settings have been added to choose RCWA parameters: number of layers, resolution of local E-field calculations, and number of Fourier modes.

```
1 function S = gp4_settings
2 ...
3 %===RCWA settings===
4 S.NL = 125;             % Total number of layers
5 S.res_x= 4;            % Resolution in nm in x direction for local field
6 S.res_y= 4;            % Resolution in nm in y direction for local field
7 S.res_z= 3;            % Resolution in nm in z direction for local field
8 S.PQ = 17;             % Number of Fourier modes (must be odd)
```